Mass-transport complexes (MTCs) document minibasin subsidence patterns and diapir evolution in the northern Gulf of Mexico

Nan Wu[1], Christopher A-L. Jackson[1], Howard D. Johnson[1], David M. Hodgson[2], Harya D. Nugraha[1]

[1]Basins Research Group (BRG), Department of Earth Science & Engineering, Imperial College, Prince Consort Road, London, SW7 2BP, UK

[2]School of Earth and Environment, University of Leeds, Leeds, LS2 9JT, UK

*Email: n.wu16@imperial.ac.uk

Abstract

Mass-transport complexes (MTCs) dominate many salt-influenced sedimentary basins. Commonly in such settings, halokinesis is invoked as the primarily trigger for MTC emplacement. Despite being very well-imaged in seismic reflection data, we know little of how MTCs vary in terms of their sedimentological character, which may relate to their provenance, or their triggers. We use high-quality 3D seismic reflection and well data to study MTCs preserved in a salt-confined, supra-canopy minibasin in the northern Gulf of Mexico to interpret six MTCs that together constitute >60% of the minibasin-fill volume. We define three main tectono-sedimentary phases in the development of the minibasin: (1) initial minibasin subsidence and passive diapirism, during which time deposition was dominated by relatively large-volume MTCs (c. 25 km^3) derived from the shelf-edge or upper slope; (2) minibasin margin uplift and steepening, during which time small-volume MTCs (c. 20 km^3), derived from the shelf-edge or upper slope, were emplaced; and (3) diapir burial and late-stage active diapirism, during which time very small volume MTCs (c. 1 km^3) were emplaced, locally derived from minibasin flanks or their roofs. We present a generic model that emphasises the dynamic nature of minibasin evolution, and how MTC emplacement relates to halokinetic sequence development. Although based on a data-rich case study, our model may be applicable to other MTC-rich, salt-influenced sedimentary basins.

Keywords: MTCs, salt mini-basins evolution, Gulf of Mexico.

Introduction

Mass-transport complexes (MTCs) are deposits of subaqueous mass flows, and comprise slides, slumps, and debris-flows (Dott Jr, 1963; Nardin et al., 1979; Posamentier and Kolla, 2003). MTCs are emplaced along all continental margins, and play a major role in sediment transfer from the continents to the deep ocean (e.g. Masson et al., 2006; Hjelstuen et al., 2007; Talling et al., 2007; Li et al., 2015). Seismically imaged MTCs can be very large (c. 20-1100 km^3) (e.g. Gee et al., 1999; Frey Martinez et al., 2005; Moscardelli et al., 2006; Sawyer et al., 2007; Moscardelli and Wood, 2008; Sawyer et al., 2009; Ortiz‐Karpf et al., 2016; Wu et al., 2019), and can constitute >50% of any given deep-water stratigraphic succession (Posamentier and Walker (2006). MTC initiation is often triggered by earthquakes and/or tsunami (Nisbet and Piper, 1998; O'loughlin and Lander, 2003), and their passage and emplacement may damage seabed infrastructure (Shipp, 2004). In the petroleum industry, MTCs can serve as hydrocarbon seals and reservoirs (Hampton et al., 1996; Locat and Lee, 2002; Weimer and Shipp, 2004; Wu et al., 2019). Understanding the causal mechanisms and morphological characteristics of MTCs is therefore important for academic and industrial reasons.

In salt-influenced sedimentary basins, salt tectonics is often considered to be the primary control on the emplacement of MTCs (e.g. Moscardelli and Wood, 2008; Madof et al., 2009). However, the relative rates of sediment input and accumulation, and accommodation creation, also dictate when and where MTCs are emplaced in salt-controlled depocentres (often referred to as 'minibasins'; Jackson and Hudec, 2017). Sediment input and accumulation rates are influenced by the location of the minibasin relative to larger-scale depositional systems, including shelf-edge deltas and upper slope canyons, or the position of the these depocentres on the slope (i.e., upper, middle, lower slope). Accommodation will dictate the volume of MTC material trapped and preserved within any minibasin, and the likelihood (or not) of sediment bypass to distal depocentres.

The stratigraphic architecture and evolution of minibasins in the Gulf of Mexico are frequently linked to the fill-and-spill model (Prather et al., 1998; Winker and Booth, 2000; Booth et al., 2003; Mallarino et al., 2006; Madof et al., 2009; Prather et al., 2012). According to this model, underfilled minibasins initially trap or 'pond' sediments, before they are overfilled, permitting sediment bypass to more distal depocentres (Beaubouef and Friedmann, 2000; Booth et al., 2000; Booth et al., 2003). Underlying this model are two major assumptions: (1) accommodation in the minibasin is controlled by a steady-state, longitudinal bathymetric profile, and (2) the minibasin gradient does not vary spatially and temporally during its evolution (Prather et al., 1998; Winker and Booth, 2000; Mallarino et al., 2006). However, Madof et al. (2009) and Madof et al. (2017) argue that these assumptions are unrealistic given that minibasins can be extremely dynamic, with their geometry, subsidence and accommodation changing in response to variations in sediment supply rate and input direction, and the rate and location of salt expulsion from beneath these subsiding depocentres. Sylvester et al. (2015) use a geometrical model to also highlight how a static temporal framework fails to reproduce the stratigraphic patterns and, more specifically, age relationships observed in natural minibasins. In addition, the fill-and-spill model has only really been applied to turbidite-dominated supply systems comprising channels and lobes; the potentially significant role of MTCs is not captured, likely because of an understandable focus on the more reservoir-prone channels and lobes.

Motivated by the above discussion, we here use 3D seismic reflection and well data from the northern Gulf of Mexico to: (i) define the geometry and emplacement mechanics of minibasin-confined MTCs; (ii) link MTC emplacement to the development of halokinetic sequences (see below) that characterise specific stages in the relationship between minibasin subsidence and diapir uplift. By doing this we can: (i) explicitly account for MTCs in dynamic minibasin fill-and-spill models; (ii) characterise the dynamic interactions between deep-water sedimentation and halokinesis; and (iii) use MTCs as markers of salt-related structural deformation in deep-water. Although we focus on a single upper slope minibasin in the northern Gulf of Mexico (Figure 1), the high-quality dataset, and the fact that salt-sediment interactions have been documented in many other sedimentary basins (e.g. Gulf of Mexico, offshore Brazil and offshore West Africa) mean our findings are likely to be broadly applicable.

Geological setting

Tectonics

The Gulf of Mexico passive continental margin formed in response to Triassic-Early Cretaceous rifting (Pindell and Dewey, 1982; Salvador, 1987; Kneller and Johnson, 2011). Rifting initiated during the Late Triassic, followed by repeated episodes of marine flooding episodes of a confined embayment during the Middle Jurassic. This led to the accumulation of the several kilometre-thick Louann Salt (Diegel et al., 1995; Salazar et al., 2014). During the Mesozoic and Cenozoic, large volumes of sediments were shed from the North American continent. This, in concert with regional shortening, expelled the autochthonous salt into diapirs that fed a large, allochthonous salt-canopy (Galloway et al., 2000). Numerous intraslope minibasins formed on the upper to middle slope during this time, in response to the differential loading by continent-derived sediment, and kinematically linked extension and shortening of the supra-salt cover (Prather, 2000). Salt tectonics has thus been a major control on the stratigraphic evolution of the northern Gulf of Mexico from the Miocene to Present (e.g. Madof et al., 2009).

Location of study area

The study area is located on the present-day northern Mississippi Slope, c. 60 km south-east of the modern shelf-edge (Figure 1). This covers the upper slope area, in a diapir- and minibasin-rich region forming part of the larger Plio-Pleistocene Mississippi Canyon/Fan System (Galloway et al., 2000). Present-day water depths range from 1150 m in the SE to 650 m in the NW. Five upper Pliocene to Holocene minibasins are imaged in our study area; we focus on the Pleistocene fill of Minibasin 5, a c. 21 km long (N-S) by 8 km wide (E-W) depocentre, whose base is c. 3600 m below the present seabed (Figure 2). Four salt diapirs bound the lateral margins of Minibasin 5 (A-D; Figure 2), whereas a fifth diapir underlies it (E; Figure 3, 4).

Dataset and methods

Seismic reflection data

The seismic reflection dataset used in this study covers an area of c. 550 km^2. The dataset was acquired in 1995-1998 and reprocessed as a single survey in 2008. It contains a 3D zero-phase, Kirchhoff pre-stack depth-migrated seismic reflection volume, with a vertical sample rate of 10 m, record length of 15 km, and a final bin size of 25 m x 25 m. The vertical seismic resolution is estimated to be c. 17-27 m (Wu et al., 2019).

We mapped nine key seismic horizons in a succession characterised by alternating packages of high-amplitude, continuous reflections, and low-amplitude, more chaotic reflections (Figure 3, 4). We mapped eight additional horizons, each of which represented the base or top surface of an MTC (e.g., H2.1, H5.1 in figure 3; see also Figures 4 and 5). We used seismic attributes (i.e., variance, chaos, RMS), generated along or between these horizons, to identify deep-water depositional elements (Chopra and Marfurt, 2007; Brown, 2011).

Well data

A slightly deviated exploration well (AT-8 #1 ST) was drilled in 1997 in the east of the study area (Figure 2), encountering a c. 3600 m-thick, Pleistocene, deep-water clastic succession (Figure 3). The well-log dataset includes gamma-ray (GR) and velocity (DT) data that we used to infer the lithology of the MTCs and their bounding strata via construction of a seismic-to-well tie (Figure 6) (Wu et al., 2019). Five MTC-bearing intervals were drilled and logged by AT-8 #1 ST. MTCs tend to have higher acoustic velocities and are more resistive than bounding strata (i.e. hemipelagites, turbidites) at similar burial depths. The MTCs are mudstone-rich, with the transported and remnant blocks they contain being relatively sandstone-rich (Wu et al., 2019).

Biostratigraphy data

Pilo-Pleistocene biostratigraphic data constrain the age of strata within, above or below the MTCs. Biostratigraphic data include foraminiferal planktonic, and benthic regional and local markers, along with regional and local calcareous nannoplanktonic markers spanning the late Pliocene to Quaternary. Twelve biostratigraphic markers were identified by the contractors; we tied these to the Biostratigraphic Chart of the Gulf of Mexico Offshore Region. The biostratigraphic data provide a relatively low-resolution age control for the Pleistocene sediments within Minibasin 5. However, these data allow us to broadly determine the main tectono-sedimentary phases of minibasin development, including the timing of MTC emplacement (Figure 3, see also Supplementary Material 1-2).

Minibasin 5

Seismic facies framework

Based on reflection amplitude (e.g. high vs. low) and continuity (e.g. stratified vs. chaotic), we identify two main seismic facies in Minibasin 5 (Figure 5). Depositional elements and processes are further interpreted based on lithology data provided by AT-8 #1 ST, together with analogue information provided by seismic reflection- and well-based analysis of similar depositional systems in adjacent areas (e.g., Prather et al., 1998; Posamentier and Kolla, 2003; Roesink et al., 2004; Sincavage et al., 2004; Madof et al., 2009; Perov and Bhattacharya, 2011; Madof et al., 2017; Wu et al., 2019). Stratified seismic facies are characterised by good reflection continuity, and are further subdivided based on reflection amplitude and geometry

(SFs1, SFs2 and SFs3; Figure 5). Overall, stratified seismic facies document a range of non-MTC depositional elements (e.g. channels, lobes, sheets) deposited by a range of processes (e.g. turbidity currents, suspension fallout). Chaotic seismic facies are characterised by discontinuous, low- to medium-amplitude reflections, and are further subdivided based on their internal reflection pattern (SFc1, SFc2 and SFc3; Figure 5). Overall, chaotic seismic facies record deposition within MTCs, emplaced by a range of MTC-related processes (e.g. slumps, slides, debris flows).

Stratigraphic framework of Minibasin 5

We have identified seven seismic units in Minibasin 5 (Figure 6). Seismic unit 1 (SU-1) is c. 460-580 m thick. SU-1 consists of sandstone-rich channels and lobes, interbedded with mudstone-rich slope deposits. Seismic unit 2 (SU-2) is c. 520-600 m thick, and comprises sandstone-rich turbidite channel complexes and mudstone-rich slope deposits (Figure 6). Seismic unit 3 (SU-3) is c. 530-640 m thick, and comprises sandstone- and mudstone-rich MTCs, mudstone-rich slope sediments, and turbidite channel-fills (Figure 6). Seismic unit 4 (SU-4) is c. 210- 290 m thick and consists exclusively of mudstone-rich slope deposits. Seismic unit 5 (SU-5) is c. 470-560 m thick, and consists mudstone-rich MTCs, sandstone-rich channel complexes, and mudstone-rich slope deposits (Figure 6). Seismic unit 6 (SU-6) is c. 320-380 m thick, and contains mudstone-rich slope deposits and sandstone-rich turbidite channel complexes. The uppermost unit, Seismic unit 7 (SU-7), is c. 520-630 m thick, and consists of sandstone- and mudstone-rich MTCs, mudstone-rich slope deposits, and sandstone-rich turbidite channel complexes.

Tectono-stratigraphic development

The seven seismic units identified above are grouped into three stages that define the tectono-sedimentary development of Minibasin 5 (Figure 6). These stages are defined by: (i) the geometrical characteristics of the main seismic packages (i.e. bowl- vs. wedge- vs. layer-shaped; see Jackson et al., 2019; see also Rowan & Weimer, 1999); (ii) the way in which stratal units terminate against bounding salt diapirs (N.B. we here use the halokinetic sequence terminological framework of Giles and Rowan (2012); (iii) the types depositional systems (e.g. channels, lobes, MTCs, etc) present; and (iv) changes in overall sediment accumulation rate.

Stage 1: Passive diapirism and minibasin downbuilding

Description:

Stage 1 consists of SU-1-3 (early-middle Pleistocene). We identify two depocentres during this stage (Figure 7a). The diapirs flanking these minibasins differ in that the western one is relatively tall and has a steep margin, whereas the eastern one is lower relief and has a more gently dipping flank (Figure 4, 8a). The minibasin fill during this stage is bowl-shaped, with individual units progressively thinning towards and onlapping onto the flanking diapirs (i.e. tapered composite halokinetic sequences of Giles & Rowan, 2012) (See figure 4b and 8a). Deposition of slope channel-fills, lobes and slope sediments appear to characterise the early fill of this stage (Unit 1-2), although at least two seismic-scale MTCs, encased in very fine-grained slope deposits (Unit 3), are identified in the upper part of the succession (Figure 6). The average sedimentation rate during stage 1 was c. 1315 m/Myr (see Figure 9).

Interpretation:

The presence of symmetrical, bowl-shaped packages indicates Minibasin 5 initially subsided vertically and was flanked by passively rising diapirs (Rowan and Weimer, 1998; Hudec et al., 2009; Jackson et al., 2019). The presence of tapered composite halokinetic sequences indicate sediment accumulation rate exceeded the diapir rise rate at this time (see also Giles and Rowan, 2012). This high sediment accumulation rate may reflect a high sediment supply rate that may itself reflect the proximity of the study area to the Mississippi River, which at this time delivered large volumes of sediment to upper slope minibasins (Figure 8a).

Stage 2: Load-driven passive salt diapirism

Description:

Stage 2 comprises seismic units 4-6 (middle-late Pleistocene). During this stage, the northern depocentre shifts eastwards, whereas the southern depocentre simply expands (Figure 7b). The western diapir is flanked by tabular (SU-4-6) composite halokinetic sequences (i.e. Giles and Rowan, 2012), and the eastern diapir are being buried by the sediments (Figure 4b, 8b). The minibasin fill during this stage is defined by broadly wedge-shaped package (See figure 3, 4, and 8b). Slope channel-fills are deposited during the early part of this stage (Unit 4), with an MTC, encased in slope mudstone (Unit 5), and ultimately, slope mudstone, intercalated with slope channel-fills (Unit 6). The average sedimentation rate increased to c. 2154 m/Ma (from c. 1315 m/Ma) during Stage 2 (see Figure 9).

Interpretation:

During Stage 2, the paleo-Mississippi River continued to deliver sediments to the upper slope minibasins (Figure 8b). The presence of wedge-shaped packages records asymmetrical minibasin subsidence, and eastwards tilting of the northern minibasin (Rowan and Weimer, 1998; Hudec et al., 2009; Jackson et al., 2019). The diapir flanking the eastern side of minibasin was eventually covered by sediment, indicating an overall transition to time during which sediment accumulation rate exceeded diapir rise rate. In contrast, the western diapir contained to passively rise as diapir rise rate exceeded sedimentation rate. This interpretation is supported by the observation that tabular CHSs are deposited along this diapir flank at this time (Figure 4b, 8b).

Stage 3: Diapir burial and late-stage active diapirism

Description:

Stage 3 comprises SU-7 (late Pleistocene). During this stage, broadly layer-shaped packages are deposited (See figure 3, 4, and 8c). Overall, the whole package gradually thins towards and extend across salt diapirs, being thickest into the minibasin centre. However, in detail, the lower package (containing MTC-4) extends across the diapir, with this being onlapped by the overlying package. The upper extends across the diapir, showing only minimal thickness changes (See figure 4b and 8c). Fine-grained slope sediments, slope channel-fills, and two MTCs are deposited during Stage 3. The average sedimentation rate at this time was the highest documented during the post-early Pleistocene history of minibasin, reaching up to c. 4615 m/Myr (see Figure 9).

Interpretation:

During Stage 3 (late Pleistocene), large amounts of sediment were delivered from the Mississippi River to the upper slope and minibasin 5 (Winker and Booth, 2000) (Figure 8c). The thickness map indicates that much of the accommodation was healed and that the flanking diapirs were buried (Figure 7c). The prevalence of layer-like stratigraphic packages during Stage 3 reflects the high sediment accumulation (and possibly supply) rate at this time, which caused broadly uniform sediment aggradation above a now-welded minibasin 5. Rowan and Weimer (1998) also interpreted that layer-shaped packages reflect relatively long-wavelength subsidence across now-welded minibasins (see also Jackson et al., 2019).

Characterisation of minibasin 5 MTCs

MTC 1

Description:

MTC 1 (119 km^2 and 25 km^3) is laterally and frontally confined by salt diapirs (Figure 10a, b). MTC 1 is 160-190 m thick, and its NW-SE-striking, south-western lateral margin defines a sharp erosional contact between remobilised sediments (SFc3) and undeformed slope sediments (SFs1 and SFs2) (Fig. 10c). Its NW-SE-striking, north-eastern lateral margin is defined by the eastern salt diapir (Figure 10b). MTC 1 is sandstone-rich, containing large (130-160 m thick), internally deformed, sandstone-rich (60-80% sandstone) blocks, intercalated with thin mudstone layers (Wu et al., 2019). The highly reflective blocks, which have long axes oriented NE, are directly underlain by an interval of weakly reflective, more deformed reflections (Figure 10d). In addition, NE-SW-striking, NW-dipping thrusts are observed within the blocks (Figure 10b, c, d).

Interpretation:

Deformation at the base of the blocks suggests they were transported within MTC 1 (see also Nardin et al., 1979; Bull et al., 2009; Alves, 2015). The orientation of the NE-SW-striking thrusts, and the NW-SE-striking lateral margins, suggest that MTC 1 was transported towards the SE. We interpret the thrusts formed due to horizontal compression of the debris flow adjacent to transported blocks. An alternative interpretation is that the thrusts record shortening at the toe of the submarine landslide. The lithology of the large blocks suggests MTC 1 was derived from an up-dip sand-rich source, such as upper slope lobes and/or channels, and/or shelf-edge delta front deposits (Wu et al., 2019). The sandstone-rich blocks may therefore have travelled c. 60 km from shelf-edge/upper slope setting. Unfortunately, benthic foraminifera, which might help confirm the original depositional setting or at least water depth of these sandstones, are lacking. We suggest, however, that blocks within MTC 1 are unlikely to have been derived from the nearby salt diapirs because, at this time, the diapirs were capped by an intact sedimentary roof comprising tapered CHS (see Figure 3 and 4).

MTC 2

Description:

MTC 2 (113.5 km^2 and 21.6 km^3) is 110-150 m thick and has a similar external geometry to MTC 1, being defined by: (i) a sharp, NW-SE-trending, erosional lateral margin on its south-western side, and (ii) NW-SE-striking diapir on its north-eastern side (Figure 11a, b). MTC 2 is mudstone-rich and contains subordinate, relatively sandstone-rich (30-40% sand) blocks that are 20-40 m thick (Wu et al., 2019). In the centre of Minibasin 5, MTC 2 contains two large (90-170 m) blocks, one of which contains mudstone-rich SFs2 at its base and sandstone-rich SFs1 at its top (Figure 11c) (Wu et al., 2019). The long axes of these blocks trend NW-SE (Figure 11b). Smaller blocks are clustered towards the north-east minibasin margin (Figure 11a, b). Unlike the transported blocks in MTC 1, blocks in MTC 2 have sharp contacts with debritic material (SFc2), are not deformed, and are not underlain by seismic-scale zones of deformation (Figure 11c).

Interpretation:

Their sharp edges, and the lack of deformation within and below them, suggests the blocks represent undeformed substrate material that was not transported within the MTC. The blocks are therefore referred to as remnant blocks (e.g. Frey Martinez et al., 2005; Bull et al., 2009). Based on the orientations of its lateral margins, we suggest MTC 2 was transported to the SE. Although there is no direct evidence (i.e. benthic foraminifera) indicating the source area of MTC 2, the presence of the subordinate sandstone-rich blocks, and similar kinematic indicators to MTC 1 (i.e. the NW-SE-trending lateral margins), together suggest MTC 2 was also derived from shelf-edge and/or upper slope.

MTC 3 & 4

Description:

MTC 3 (123.5 km^2 and 20.3 km^3) is 110-160 m thick, and has a similar external geometry to MTC 1 and 2, bounded by: (i) a NW-SE-trending trending erosional margin on its south western side, and (ii) NW-SE-striking diapir on its north-eastern side (Figure 12a, b). MTC 3 is mudstone-dominated and contains sandstone-rich blocks (c. 20-40% sand) that are 30-60 m thick (Wu et al., 2019). Biostratigraphic data indicate MTC 3 contains transported outer shelf sediments (2377 m; see figure 13). Two biostratigraphic samples collected from a slightly deeper position, at 2487 m, give an age of 0.78 and 0.85 Ma (lower Pleistocene; Figure 12c, 13).

MTC 4 (98.4 km^2 and 18.1 km^3) has a similar geometry to the underlying MTCs, being again defined by: (i) a NW-SE-trending lateral margin on its south-western side, and (ii) NW-SE-striking diapir on its north-eastern side (Figure 14a, b). MTC 4 is mudstone-rich and 70-110 m thick (Figure 6), and contains remnant blocks, the long axes of which trend NW-SE (Figure 13b).

Interpretation:

The orientations of their lateral margins suggest that MTC 3 and 4 were transported towards the SE (e.g. Frey Martinez et al., 2005; Bull et al., 2009). MTC 3 contains direct biostratigraphic evidence it was derived from the paleo shelf-edge (i.e. transported outer shelf facies sample; Figure 10). The presence of two different age samples (0.78 and 0.85 Ma) from the same depth (2478 m) is intriguing. This might indicate that an MTC at 0.78 Ma (i.e. MTC 3) entrained older (i.e. 0.85 Ma) substrate (i.e. seabed) material during transport and emplacement (Figure 13d). An alternative interpretation is that relatively old (i.e. 0.85 Ma) material was shed from the roof of a growing diapir flanking the minibasin, being reworked into the younger (i.e. 0.78 Ma) stratigraphy (Figure 13e). As MTC 4 is similar to older MTCs in terms of its geometry and kinematics, it was also likely derived from the upper slope or paleo shelf-edge.

MTC 5

Description:

MTC 5 (29.07 km^2 and 2.6 km^3) is 110-180 m thick and was deposited in the centre of Minibasin 5, being bounded by diapirs on its NE and W and salt-related structure high on its SE (Figure 15a, b). MTC 5 is sandstone-rich and is intercalated with thin mudstone layers. Sandstone-rich blocks (c. 40-60% sand) that are 60-90 m thick occur within MTC 5. We sub-divide MTC 5 into MTC 5.1 and MTC 5.2, based on cross-cutting relationships between the lateral margins of the two units, with MTC 5.2 being slightly younger than MTC 5.1 (Figure 15b, d). MTC 5.1 is delineated by a set of NE-SW-striking normal faults and NE-SW-striking thrusts in its proximal and distal parts, respectively (Figure 15b). The NE-SW-striking imbricate thrusts in the seismic section (Figure 15c). MTC 5.2 has a NE-trending headwall scarp, being bound by NW-SE-striking lateral margins. Well AT-8 #1 ST intersected MTC 5.1, which is sandstone-rich (Figure 6). However, well AT-8 #1 ST does not penetrate on MTC 5.2, thus its lithology is unknown.

Interpretation:

The strike of the normal faults and thrusts suggest bulk movement of MTC 5.1 was towards the E (e.g. Frey Martinez et al., 2005; Bull et al., 2009). The orientation of the headwall scarp and lateral margins suggest that MTC 5.2 was transported to the SE (e.g. Bull et al., 2009). The confined nature of MTC 5.1 and 5.2 suggest they were both sourced from locally positive topography generated by an underlying salt diapir.

MTC 6

Description:

MTC 6 (18.9 km^2 and 1.13 km^3) is located just below the seabed along the south-eastern flank of salt diapir A, which bounds the south-western margin of Minibasin 5 (Figure 16a, b). MTC 6 has well-defined NW-SE-trending lateral margins and is 50-70 m thick. In the up-dip part of MTC 6, the N-S-striking normal faults occur on the flank of the diapir, with the strata thickening into the hanging walls of the normal faults (Figure 16c). N-S-striking thrusts are also developed near the north-eastern lateral margin of MTC 6 (Figure 16a, b). The north-eastern lateral margin of MTC 6 is erosional, with the magnitude of erosion increasing towards the northeast. MTC 6 pinches-out to the southwest (Figure 16d). The N-S-striking normal faults and thrusts are present above the main body of MTC 6 (Fig. 16e). AT-8 #1 ST does not penetrate MTC 6, thus its lithology is unknown.

Interpretation:

The orientations of the normal faults and the lateral margins suggest MTC 6 was transported to the SE. These spatial relationships suggest that MTC 6 was triggered by gravity-driven instability of the seabed, driven by uplift of the seabed by diapir A. The emplacement of MTC 6 created an exposed and unstable lateral margin along its NE side (Figure 16d, f). This margin thus collapsed, depositing material on top of the main body of the MTC 6 (Figure 16g).

Discussion

Origin and classification of MTCs

Moscardelli and Wood (2008) classify MTCs in salt-confined minibasins as ‘detached’ (i.e. originating from and still partly physically connected to a local source, such as a salt-cored structural high). However, we find that minibasin-hosted MTCs can also be ‘attached’, having been sourced, but now being physically disconnected from, the relatively distal shelf-edge or upper slope. Here, we provide additional guidelines on how to differentiate between attached and detached MTCs in salt-confined minibasin settings, focusing on: (i) MTC morphometrics (i.e. external geometry, area, volume); (ii) the composition and age of the MTCs; and (iii) the geometrical relationship between the MTCs and bounding salt diapirs (see Figure 17).

Shelf-edge/upper slope derived MTCs (MTC 1-4)

The shelf-edge-/upper slope-derived MTCs tend to be overall larger than the diapir-derived MTCs (i.e. 110-270 m thick; 113.5 to 123.5 km^2 in area; 20.3 to 25.1 km^3 in volume). These MTCs are most common during the initial phase of minibasin development (i.e. Stage 1 and 2; early to middle Pleistocene) (Figure 18). They are thickest near the minibasin centre, with their parent flows transported sediment to the SE, along a bathymetric low laterally bound by salt diapirs. Shelf-edge-/upper slope-derived MTCs can be sandstone- or mudstone-rich, and typically contain sandstone-rich blocks. We infer these MTCs were sourced from the collapse of coeval shelf-edge deltas, and/or we supplied by reworked upper slope channels and lobes. The trigger for slope failure and MTC emplacement is unknown.

Diapir-derived MTCs (MTC 5-6)

Diapir-derived MTCs tend to be overall smaller than shelf-edge-/upper slope-derived MTCs (i.e. 50-90 m thick; 18.9 to 29.7 km^2 in area; 1.13 to 2.6 km^3 in volume). Diapir-derived MTCs were emplaced during the latter stage of minibasin development (Stage 3; late Pleistocene) (Figure 18). These MTCs are preserved on or immediately downdip of, the flanks of diapirs (i.e. MTC 6) or on locally positive topography created by underlying diapirs (i.e. MTC 5). Diapir-derived MTCs are thickest near diapir margins and thin downdip into the centre of the minibasin, indicating local derivation from above or the flanks of diapir-cored structural highs. It is likely that emplacement of this type of MTC is linked to localised gravitational instability, more specifically oversteepening of diapir flanks during passive or active diapirism (discussed below).

Minibasin evolution; beyond the fill-and-spill model

The widely utilised fill-and-spill model has two key assumptions: (i) the longitudinal gradient between two (or more) adjacent minibasins does not vary through time; and (ii) sedimentation rate always exceeds the rate of minibasin subsidence (Beaubouef and Friedmann, 2000; Booth et al., 2000; Booth et al., 2003). In this model, minibasins evolve from ponded, through perched, and finally, to bypass (Beaubouef and Friedmann, 2000). The conventional fill-and-spill model typically only considers turbidite-dominated supply systems; the role of MTCs is not explicitly considered (i.e. Prather et al., 1998; Winker and Booth, 2000; Sinclair and Tomasso, 2002; Mallarino et al., 2006).

Several studies show that the longitudinal gradients and the seabed bathymetry changes through time due to the way in which minibasins subside, and because of changes in the ratio of accommodation creation and sediment supply/accumulation rate (e.g. Madof et al., 2009; Sylvester et al., 2015; Madof et al., 2017). Thus, the original fill-and-spill model is overly simplistic. Madof et al. (2017) propose a process-driven model of 'subsidence and margin failure' for minibasin evolution; this better accounts for the seismic-stratigraphic architecture of minibasins compared to the fill-and-spill model. In their model, rising diapirs pond sediments within minibasins (Stage 1). The ponded sediments then promote minibasin subsidence (due to density-driven downbuilding) and basin margin uplift (due to passive diapirism) (Stage 2). Margin uplift leads to slope oversteepening, failure, and generation of intra-basinal MTCs (Stage 3). Although this model is suitable for intra-basinal MTCs (i.e. derived from salt minibasin margins), it does not address how extra-basinal, shelf-edge-/upper slope-derived MTCs are emplaced in a minibasin. Thus, we here extend their model by taking halokinesis, subsidence and sedimentation into consideration, using our observations from the northern Gulf of Mexico, in which MTCs constitute c. 60% of the minibasin fill.

We have identified three key stages during the evolution of minibasin 5: (i) an initial stage (Stage 1) characterised by relatively low sedimentation rates (1316 m/Myr), passive diapirism, and broadly vertical subsidence of the minibasin, resulting in the deposition of tapered composite halokinetic sequences. Sandstone-rich slope channel complexes and lobes, as well as sandstone-rich, shelf-edge/upper slope-derived MTCs, were deposited in the minibasin at this time (Figure 18). These extra-basinal MTCs were relatively large (i.e. 25 km^3) and were deposited in the deepest, central point of the minibasin. MTC emplacement was associated with substantial substrate deformation; (ii) a subsequent stage (Stage 2) characterised by relatively high sedimentation rates (2645 m/Myr), during which time the rate of (passive) diapir rise exceeded the sediment accumulation rate, resulting in the deposition of tabular composite halokinetic sequences. Stage 2 was characterized by emplacement of mudstone-rich, shelf-edge-derived MTCs (i.e. MTC 3), sandstone-rich slope-channel fills, and mudstone-rich slope deposits (Figure 18). Stage 2 MTCs are geometrically similar to Stage 1 MTCs, but were smaller (i.e. 1.13km^3); (iii) a final stage (Stage 3) characterised by the highest sedimentation rates (4615 m/Myr), during which time sedimentation rate exceeded the rate of diapir rise, resulting in capping of the minibasin-bounding diapirs by a relatively thick roof. Stage 3 saw deposition of sandstone-rich slope-channel fills and lobes, and sandstone-rich, diapir-derived MTCs (Figure 18). These relatively small (i.e. 1.13km^3), intra-basinal MTCs were sourced from and deposited proximal to, the flanks of rising salt diapirs.

Our model develops the existing minibasin evolution model of Madof et al. (2009), showing that: (i) the interplay between the relative rate of salt movement, minibasin subsidence and sediment accumulate rate dictates the geometry of the deposits within the minibasin; (ii) MTCs play a fundamental role in the different stages of minibasin fill; and (iii) the style of salt-related structural deformation can be determined by the volume and type of coeval MTC(s).

Controls on the emplacement of detached MTCs

Eustasy

Eustasy controls depositional processes and stratal patterns along basin margins (e.g., Vail et al., 1977; Posamentier et al., 1988; Catuneanu, 2002; Posamentier and Kolla, 2003; Catuneanu et al., 2011). Eustacy was particularly important during the Pleistocene in the northern Gulf of Mexico, when rapid (c. 500 years), high-amplitude (>100 m) sea-level fluctuations resulted in rapid margin progradation and retrogradation (Galloway, 2001). For example, Pleistocene sea level fluctuations are known to have caused major changes in the position of the paleo-coastline (>100 km) during glacial intervals (Galloway et al., 2011).

During periods of sea-level fall, sediment supply was so high that deltas could reach the shelf-edge. Rapid progradation during periods of sea-level fall and lowstand could generate an increase of pore-fluid pressure because low permeability, mudstone-rich slope sediments cannot efficiently expel their pore water when loaded by thick, shelf-edge deltas (Madof et al., 2017). This can trigger failure of the shelf-edge or upper slope, and the emplacement of MTCs (Posamentier and Kolla, 2003).

There were numerous and frequent, glacio-eustatic sea-level fluctuations during the Pleistocene in the Gulf of Mexico (Figure 19). It may thus be appealing to link MTC emplacement to periods of falling and lowstands of sea level, via the causal mechanism outlined above. However, we note there were many more falls than there are seismically resolvable MTCs in minibasin 5. Any MTCs generated during periods of sea-level fall may have: (i) been ponded in up-dip minibasins; (ii) transformed into turbidity currents and bypassed Minibasin 5 downdip; and (iii) been emplaced in a minibasin lateral to Minibasin 5.

Sedimentation

Alternatively, MTC emplacement may have been controlled by sediment supply; i.e. during periods of high supply, which may have been climatically controlled, deltas may have reached the shelf-edge even during highstands, before collapsing to supply MTCs. In the northern Gulf of Mexico, Pleistocene sedimentation rates were extremely high, and more than double Pliocene rates (Molnar, 2004). This increase is due to the greater discharge and entrenchment of the Mississippi River, related to its capture of the Ohio and Missouri rivers (Galloway et al., 2011). The reorganisation of the Mississippi River System resulted in a significant increase in basinward sediment supply and led to the development of submarine canyons that incised the shelf, especially during periods of glacial retreat (Galloway et al., 2000; Rittenour et al., 2007; Galloway et al., 2011; Bentley Sr et al., 2016). High sedimentation input from the Mississippi River caused rapid shelf-edge delta progradation. This also contributed to increasing delta front instability and the triggering of gravity-driven sediment flows (e.g., Sydow et al., 2003; Moscardelli et al., 2006). The high sedimentation rates associated with paleo-Mississippi River System are also considered to have been a key factor in triggering the shelf-edge/upper slope derived MTCs in the study area.

The link between composite halokinetic sequences and MTCs

Halokinetic sequences are defined as "unconformity-bound packages of thinned and deformed strata adjacent to passive diapirs" (Rowan et al., 2003). Halokinetic sequences represent cycles of passive diapirsm and minor active diapirism when salt periodically rises and pierces the diapir roof (Rowan et al., 2003). Halokinetic sequences form as the rate of net vertical diapiric rise varies relative to the local rate of sediment accumulation (Giles and Lawton, 2002; Rowan et al., 2003). Within this conceptual framework, diapir-derived MTCs are most likely to be emplaced in tabular composite halokinetic sequences, being generated by break-up of the diapir roof a period when diapir rise rate exceeds sediment accumulation rate (Giles and Rowan, 2012). Diapir-derived MTCs are thought to only extend a few hundred metres away from their source diapirs (i.e. Giles and Rowan, 2012; Hearon et al., 2014).

Our observations are consistent with the outcrop based model of Giles and Rowan (2012), in that the intra-basinal MTCs (diapir-derived MTCs) are best-developed in Stage 3, when tabular CHSs were deposited. However, we show that diapir-derived MTCs (i.e. MTC 6) can extend > 8 km away from their source diapir. Moreover, during the initial stage of subsidence of Minibasin 5, the extra-basinal MTCs (shelf-edge /upper slope derived MTCs) were deposited in tapered CHSs. Salt diapirs provide physical bounding constraints for the distribution of the extra-basinal MTCs (e.g. MTC 1 and 2), but play no role in the triggering of these deposits. Thus, during different stages of the evolution of a minibasin, halokinetic sequences could have different relationships with their associated MTCs.

Conclusions

1. Six MTCs comprise around 60% of the basin fill in the Pleistocene salt confined Minibasin 5 in the northern Mississippi slope, Gulf of Mexico.
2. Minibasin evolution during the Pleistocene has been divided into three different stages, reflecting differences in sedimentation rates and salt halokinesis: (i) initiation of minibasin subsidence and passive diapirism by sediment loading; (ii) sedimentation driven active salt diapirism; and (iii) Diapir burial and late-stage active diapirism.
3. Two types of MTC are recognized based on their geometry, volume, and source area: (i) shelf-edge/upper slope-derived MTCs (extra-basinal) are larger-scale features (98.4-123 km^2 in area, 18.1-25 km^3 in volume, 110-270 m in thickness); (ii) diapir-derived MTCs (intra-basinal) are smaller-scale features (18.9-29.7 km^2 in area, 1.13-

2.6 km^3 in volume, 50-90 m in thickness). The former were derived from the paleoshelf-edge or upper slope areas and probably triggered by a combination of high sedimentation rates and fluctuations in relative sea level, and the latter were derived from adjacent salt flanks and/or salt-related structure highs and probably triggered by localized salt movement.

4. Shelf-edge/upper slope-derived MTCs were preferentially deposited during the first and second stages of minibasin evolution, when sediment accumulation rates were higher than the rates of diapir rise. During this time, and diapirs mainly constrained the distribution of MTCs, but were not involved in their triggering. Diapir-derived MTCs were mainly deposited during the late stage of minibasin evolution, when salt diapir rise rate was lower than sediment accumulation rate.

Acknowledgements

We thank MultiKlient Invest AS's ("PGS"), in particular Don Herron and Scott Opdyke, for providing the subsurface dataset and allowing the publication of the paper. We also thank Michael Steventon for helpful discussions throughout the duration of this work.

Figure Captions

Figure 1. Location map of the study area relative to the globe map (left) and the study area (right), showing the position of the modern shelf-edge (black dotted line), paleo-shelf-edge (white dotted line), and modern depositional systems. Bathymetry (coloured) and northern Gulf Coastal Plain topography (blue and white) of the Gulf of Mexico region. The study area (see yellow box) is located in the upper continental slope of the northern Gulf of Mexico out along the SW distal edge of the Mississippi Canyon. The location of the Pleistocene-shelf edge is from Galloway et al. (2011), the Northern Gulf of Mexico Deepwater Bathymetry map is modified from The Bureau of Ocean Energy Management (BOEM).

Figure 2. Depth map (Depth below seabed) for top salt, showing the overall salt-tectonic structure of the study area. 1-5 and A-C refer to minibasins and salt structures, respectively, described in the text. See location from figure 1.

Figure 3. (a) N-trending un-interpreted seismic section. (b) Interpreted N-trending seismic section showing the overall salt-tectonic structure of the study area, the eight key seismic horizons (H0 to seabed) and main MTC-bearing intervals (MTC 1 to MTC 6). See location from figure 2.

Figure 4. (a) W-trending un-interpreted seismic section. (b) Interpreted W-trending seismic section showing the overall salt-tectonic structure of the study area, the eight key seismic horizons (H0 to seabed) and main MTC-bearing intervals (MTC 1 to MTC 5). See location from figure 2.

Figure 5. Main seismic facies summary, six seismic facies recognized in this study shown in seismic section. A brief interpretation of the seismic facies, log facies, lithology, and facies characteristics are provided on the figure. See the text for detailed descriptions.

Figure 6. Correlation charts for the study area showing well logs (GR, Sonic, and ATR), interpreted lithology, well correlated seismic section, key horizons, and geological age of each episodes.

Figure 7. (a) Thickness map between horizon H0 and horizon H4, showing: (i) the thickness variation of minibasin evolution stage 1; and (ii) the southern and northern depocentres (labelled number 1 and 2). (b) Thickness map between horizon H4 and horizon H7, showing: (i) the thickness variation of minibasin evolution stage 2; and (ii) the southern and northern depocentres (labelled number 1 and 2). (c) Thickness map between horizon H7 and horizon seabed, showing the thickness variation of minibasin evolution stage 3.

Figure 8. Cartoons of Minibasin 5 evolution model: (a) Passive diapirism and minibasin downbuilding; (b) Sedimentation driven active salt diapirism; (c) Diapir burial and late-stage active diapirism.

Figure 9. Burial curve of Minibasin 5, showing three stages of minibasin evolution: (i) Stage 1 – 1315 m/Myr; Stage 2 – 2645 m/Myr; Stage 3 – 4615 m/Myr.

Figure 10. (a) Variance attribute calculated for the interval between the H2 and H2.1 seismic horizons, showing the plain view of MTC 1; (b) Sketch of MTC 1 indicating key kinematic features associated with MTC 1; (c) E oriented seismic section of MTC 1; (d) NNE trending seismic section of MTC 1. See location from figure10a.

Figure 11 (a) Variance attribute calculated for the interval between the H3 and H4 seismic horizons, showing the plain view of MTC 2; (b) Sketch of MTC 2 indicating key features associated with this MTC; (c) SE oriented seismic section of MTC 2, see location from figure 11a.

Figure 12 (a) Chaos attribute calculated for the interval between the H5 and H5.1 seismic horizons, showing the plain view of MTC 3; (b) Sketch of MTC 3 indicating key features associated with this MTC; (c) NNE oriented seismic section of MTC 3; (d) Sketch of MTC 3 showing the emplacement of this MTC from shelf-edge; (e) Sketch of MTC 3 showing the emplacement process from the uplift of salt diapirs. See location from figure 12a.

Figure 13. Biostratigraphy data compilation showing the age of six MTCs bearing intervals in the study area.

Figure 14 (a) RMS attribute calculated for the interval between the H7.1 and 7.2 seismic horizons, showing the map view of MTC 4; (b) Sketch of MTC 4 indicating key features associated with this MTC.

Figure 15 (a) Variance attribute calculated for the interval between H7.3, 7.4 seismic horizons, showing the map view of MTC 5; (b) Sketch of MTC 5 indicating key features associated with this MTC; (c) NE trending seismic section of MTC 5; (d) NW-NE trending seismic section of MTC 5. See location from figure 15a.

Figure 16 (a) RMS attribute calculated for the interval between the H7.5 and H7.6 seismic horizons, showing the map view of MTC 6; (b) Sketch of MTC 6 indicating key features associated with this MTC; (c) NW trending seismic section of MTC 6; (d) NE trending seismic section of MTC 6; (e) S trending seismic section of MTC 6; (f) Sketch of MTC 6 showing the first stage of emplacement; (g) Sketch of MTC 6 showing the second stage of emplacement. See location from figure 16a.

Figure 17. Schematic 3D view of three different types of MTCs observed around the study area: (i) Shelf-edge derived MTCs (SED); (ii) Upper slope derived MTCs (USD); and (iii) Diapir-derived MTCs (DD).

Figure 18. Conceptual model for extrabasinal mass transport complexes (MTCs), intrabasinal MTCs, slope channels, and background slope sediments.

Figure 19. Eustatic sea level curve for Pleistocene and Holocene from Imbrie et al. (1984) correlated with a general age of the MTCs.

Reference

Alves, T. M., 2015, Submarine slide blocks and associated soft-sediment deformation in deep-water basins: a review: Marine and Petroleum Geology, v. 67, p. 262-285.

Beaubouef, R., and S. Friedmann, 2000, High resolution seismic/sequence stratigraphic framework for the evolution of Pleistocene intra slope basins, western Gulf of Mexico: depositional models and reservoir analogs: Deep-water reservoirs of the world: Gulf Coast Section SEPM 20th Annual Research Conference, p. 40-60.

Bentley Sr, S., M. Blum, J. Maloney, L. Pond, and R. Paulsell, 2016, The Mississippi River source-to-sink system: Perspectives on tectonic, climatic, and anthropogenic influences, Miocene to Anthropocene: Earth-Science Reviews, v. 153, p. 139-174.

Booth, J., A. DuVernay III, D. Pfeiffer, and M. Styzen, 2000, Sequence stratigraphic framework, depositional models, and stacking patterns of ponded and slope fan systems in the Auger Basin: Central Gulf of Mexico slope: Perkins Research Conference, p. 82-103.

Booth, J. R., M. C. Dean, A. E. DuVernay III, and M. J. Styzen, 2003, Paleo-bathymetric controls on the stratigraphic architecture and reservoir development of confined fans in the Auger Basin: central Gulf of Mexico slope: Marine and Petroleum Geology, v. 20, p. 563-586.

Brown, A. R., 2011, Interpretation of three-dimensional seismic data, Society of Exploration Geophysicists and American Association of Petroleum Geologists.

Bull, S., J. Cartwright, and M. Huuse, 2009, A review of kinematic indicators from mass-transport complexes using 3D seismic data: Marine and Petroleum Geology, v. 26, p. 1132-1151.

Catuneanu, O., 2002, Sequence stratigraphy of clastic systems: concepts, merits, and pitfalls: Journal of African Earth Sciences, v. 35, p. 1-43.

Catuneanu, O., W. E. Galloway, C. G. S. C. Kendall, A. D. Miall, H. W. Posamentier, A. Strasser, and M. E. Tucker, 2011, Sequence stratigraphy: methodology and nomenclature: Newsletters on stratigraphy, v. 44, p. 173-245.

Chopra, S., and K. J. Marfurt, 2007, Seismic attributes for prospect identification and reservoir characterization, Society of Exploration Geophysicists and European Association of Geoscientists and Engineers.

Diegel, F. A., J. Karlo, D. Schuster, R. Shoup, and P. Tauvers, 1995, Cenozoic structural evolution and tectono-stratigraphic framework of the northern Gulf Coast continental margin.

Dott Jr, R., 1963, Dynamics of subaqueous gravity depositional processes: AAPG Bulletin, v. 47, p. 104-128.

Frey Martinez, J., J. Cartwright, and B. Hall, 2005, 3D seismic interpretation of slump complexes: examples from the continental margin of Israel: Basin Research, v. 17, p. 83-108.

Galloway, W. E., 2001, Cenozoic evolution of sediment accumulation in deltaic and shore-zone depositional systems, northern Gulf of Mexico Basin: Marine and Petroleum Geology, v. 18, p. 1031-1040.

Galloway, W. E., P. E. Ganey-Curry, X. Li, and R. T. Buffler, 2000, Cenozoic depositional history of the Gulf of Mexico basin: AAPG bulletin, v. 84, p. 1743-1774.

Galloway, W. E., T. L. Whiteaker, and P. Ganey-Curry, 2011, History of Cenozoic North American drainage basin evolution, sediment yield, and accumulation in the Gulf of Mexico basin: Geosphere, v. 7, p. 938-973.

Gee, M., D. Masson, A. Watts, and P. Allen, 1999, The Saharan debris£ ow: an insight into the mechanics of long runout submarine debris£ ows: Sedimentology, v. 46, p. 317-335.

Giles, K. A., and T. F. Lawton, 2002, Halokinetic sequence stratigraphy adjacent to the El Papalote diapir, northeastern Mexico: AAPG bulletin, v. 86, p. 823-840.

Giles, K. A., and M. G. Rowan, 2012, Concepts in halokinetic-sequence deformation and stratigraphy: Geological Society, London, Special Publications, v. 363, p. 7-31.

Hampton, M. A., H. J. Lee, and J. Locat, 1996, Submarine landslides: Reviews of geophysics, v. 34, p. 33-59.

Hearon, T. E., M. G. Rowan, K. A. Giles, and W. H. Hart, 2014, Halokinetic deformation adjacent to the deepwater Auger diapir, Garden Banks 470, northern Gulf of Mexico: Testing the applicability of an outcrop-based model using subsurface data: Interpretation, v. 2, p. SM57-SM76.

Hjelstuen, B. O., O. Eldholm, and J. I. Faleide, 2007, Recurrent Pleistocene mega-failures on the SW Barents Sea margin: Earth and Planetary Science Letters, v. 258, p. 605-618.

Hudec, M. R., M. P. Jackson, and D. D. Schultz-Ela, 2009, The paradox of minibasin subsidence into salt: Clues to the evolution of crustal basins: Geological Society of America Bulletin, v. 121, p. 201-221.

Imbrie, J., J. D. Hays, D. G. Martinson, A. McIntyre, A. C. Mix, J. J. Morley, N. G. Pisias, W. L. Prell, and N. J. Shackleton, 1984, The orbital theory of Pleistocene climate: support from a revised chronology of the marine d18O record.

Jackson, C. A.-L., O. B. Duffy, N. Fernandez, T. Dooley, M. Hudec, M. Jackson, and G. Burg, 2019, The Stratigraphic Record of Minibasin Subsidence.

Jackson, M. P., and M. R. Hudec, 2017, Salt tectonics: Principles and practice, Cambridge University Press.

Kneller, E. A., and C. A. Johnson, 2011, Plate kinematics of the Gulf of Mexico based on integrated observations from the Central and South Atlantic.

Li, W., T. M. Alves, S. Wu, D. Völker, F. Zhao, L. Mi, and A. Kopf, 2015, Recurrent slope failure and submarine channel incision as key factors controlling reservoir potential in the South China Sea (Qiongdongnan Basin, South Hainan Island): Marine and Petroleum Geology, v. 64, p. 17-30.

Locat, J., and H. J. Lee, 2002, Submarine landslides: advances and challenges: Canadian Geotechnical Journal, v. 39, p. 193-212.

Madof, A. S., N. Christie-Blick, and M. H. Anders, 2009, Stratigraphic controls on a salt-withdrawal intraslope minibasin, north-central Green Canyon, Gulf of Mexico: Implications for misinterpreting sea level change: AAPG bulletin, v. 93, p. 535-561.

Madof, A. S., N. Christie-Blick, M. H. Anders, and L. A. Febo, 2017, Unreciprocated sedimentation along a mud-dominated continental margin, Gulf of Mexico, USA: Implications for sequence stratigraphy in muddy settings devoid of depositional sequences: Marine and Petroleum Geology, v. 80, p. 492-516.

Mallarino, G., R. T. Beaubouef, A. W. Droxler, V. Abreu, and L. Labeyrie, 2006, Sea level influence on the nature and timing of a minibasin sedimentary fill (northwestern slope of the Gulf of Mexico): AAPG bulletin, v. 90, p. 1089-1119.

Masson, D., C. Harbitz, R. Wynn, G. Pedersen, and F. Løvholt, 2006, Submarine landslides: processes, triggers and hazard prediction: Philosophical Transactions of the Royal Society A: Mathematical, Physical and Engineering Sciences, v. 364, p. 2009-2039.

Molnar, P., 2004, Late Cenozoic increase in accumulation rates of terrestrial sediment: How might climate change have affected erosion rates?: Annu. Rev. Earth Planet. Sci., v. 32, p. 67-89.

Moscardelli, L., and L. Wood, 2008, New classification system for mass transport complexes in offshore Trinidad: Basin Research, v. 20, p. 73-98.

Moscardelli, L., L. Wood, and P. Mann, 2006, Mass-transport complexes and associated processes in the offshore area of Trinidad and Venezuela: AAPG bulletin, v. 90, p. 1059-1088.

Nardin, T. R., F. Hein, D. S. Gorsline, and B. Edwards, 1979, A review of mass movement processes sediment and acoustic characteristics, and contrasts in slope and base-of-slope systems versus canyon-fan-basin floor systems.

Nisbet, E. G., and D. J. Piper, 1998, Giant submarine landslides: Nature, v. 392, p. 329-330.

O'loughlin, K. F., and J. F. Lander, 2003, Caribbean tsunamis: a 500-year history from 1498-1998, v. 20, Springer Science & Business Media.

Ortiz‐Karpf, A., D. M. Hodgson, C. A. L. Jackson, and W. D. McCaffrey, 2016, Mass‐Transport Complexes as Markers of Deep‐Water Fold‐and‐Thrust Belt Evolution: Insights from the Southern Magdalena Fan, Offshore Colombia: Basin Research.

Perov, G., and J. P. Bhattacharya, 2011, Pleistocene shelf-margin delta: Intradeltaic deformation and sediment bypass, northern Gulf of Mexico: AAPG bulletin, v. 95, p. 1617-1641.

Pindell, J., and J. F. Dewey, 1982, Permo‐Triassic reconstruction of western Pangea and the evolution of the Gulf of Mexico/Caribbean region: Tectonics, v. 1, p. 179-211.

Posamentier, H., M. Jervey, and P. Vail, 1988, Eustatic controls on clastic deposition I—conceptual framework.

Posamentier, H., and R. Walker, 2006, Deep-water turbidites and submarine fans. Facies Models Revisited: Special Publication-Society for Sedimentary Geology, v. 84, p. 399-520.

Posamentier, H. W., and V. Kolla, 2003, Seismic geomorphology and stratigraphy of depositional elements in deep-water settings: Journal of Sedimentary Research, v. 73, p. 367-388.

Prather, B., 2000, Calibration and visualization of depositional process models for above-grade slopes: a case study from the Gulf of Mexico: Marine and Petroleum Geology, v. 17, p. 619-638.

Prather, B. E., J. R. Booth, G. S. Steffens, and P. A. Craig, 1998, Classification, lithologic calibration, and stratigraphic succession of seismic facies of intraslope basins, deep-water Gulf of Mexico: AAPG bulletin, v. 82, p. 701-728.

Prather, B. E., C. Pirmez, C. D. Winker, M. Deptuck, and D. Mohrig, 2012, Stratigraphy of linked intraslope basins: Brazos-Trinity system western Gulf of Mexico: Application of the principles of seismic geomorphology to continental-slope and base-of-slope systems: Case studies from seafloor and near-seafloor analogues: SEPM, Special Publication, v. 99, p. 83-109.

Rittenour, T. M., M. D. Blum, and R. J. Goble, 2007, Fluvial evolution of the lower Mississippi River valley during the last 100 ky glacial cycle: Response to glaciation and sea-level change: GSA Bulletin, v. 119, p. 586-608.

Roesink, J. G., P. Weimer, and R. Bouroullec, 2004, Sequence stratigraphy of Miocene to Pleistocene sediments of east-central Mississippi canyon, northern Gulf of Mexico.

Rowan, M. G., T. F. Lawton, K. A. Giles, and R. A. Ratliff, 2003, Near-salt deformation in La Popa basin, Mexico, and the northern Gulf of Mexico: A general model for passive diapirism: AAPG bulletin, v. 87, p. 733-756.

Rowan, M. G., and P. Weimer, 1998, Salt-sediment interaction, northern Green Canyon and Ewing bank (offshore Louisiana), northern Gulf of Mexico: AAPG bulletin, v. 82, p. 1055-1082.

Salazar, J. A., J. H. Knapp, C. C. Knapp, and D. R. Pyles, 2014, Salt tectonics and Pliocene stratigraphic framework at MC-118, Gulf of Mexico: An integrated approach with application to deep-water confined structures in salt basins: Marine and Petroleum Geology, v. 50, p. 51-67.

Salvador, A., 1987, Late Triassic-Jurassic paleogeography and origin of Gulf of Mexico basin: AAPG Bulletin, v. 71, p. 419-451.

Sawyer, D. E., P. B. Flemings, B. Dugan, and J. T. Germaine, 2009, Retrogressive failures recorded in mass transport deposits in the Ursa Basin, Northern Gulf of Mexico: Journal of Geophysical Research: Solid Earth, v. 114.

Sawyer, D. E., P. B. Flemings, R. C. Shipp, and C. D. Winker, 2007, Seismic geomorphology, lithology, and evolution of the late Pleistocene Mars-Ursa turbidite region, Mississippi Canyon area, northern Gulf of Mexico: AAPG bulletin, v. 91, p. 215-234.

Shipp, R. C., 2004, Physical Characteristics and Impact of Mass Transport Complexes on Deepwater Jetted Conductors and Suction Anchor Piles.

Sincavage, R., P. Weimer, and R. Bouroullec, 2004, Sequence Stratigraphy of Upper-Miocene to Pleistocene Sediments of Southwestern Mississippi Canyon and Northwestern Atwater Valley, Northern Gulf of Mexico.

Sinclair, H., and M. Tomasso, 2002, Depositional evolution of confined turbidite basins: Journal of Sedimentary Research, v. 72, p. 451-456.

Sydow, J., J. Finneran, A. P. Bowman, H. Roberts, N. Rosen, R. Fillon, and J. Anderson, 2003, Stacked shelf-edge delta reservoirs of the Columbus Basin, Trinidad, West Indies: Shelf-Margin Deltas and Linked Downslope Petroleum Systems, p. 441-465.

Sylvester, Z., A. Cantelli, and C. Pirmez, 2015, Stratigraphic evolution of intraslope minibasins: Insights from surface-based model: AAPG Bulletin, v. 99, p. 1099-1129.

Talling, P. J., L. A. Amy, and R. B. Wynn, 2007, New insight into the evolution of large - volume turbidity currents: comparison of turbidite shape and previous modelling results: Sedimentology, v. 54, p. 737-769.

Vail, P. R., R. Mitchum Jr, and S. Thompson III, 1977, Seismic Stratigraphy and Global Changes of Sea Level: Part 4. Global Cycles of Relative Changes of Sea Level.: Section 2. Application of Seismic Reflection Configuration to Stratigraphic Interpretation.

Weimer, P., and C. Shipp, 2004, Mass transport complex: musing on past uses and suggestions for future directions: Offshore Technology Conference.

Winker, C. D., and J. R. Booth, 2000, Sedimentary dynamics of the salt-dominated continental slope, Gulf of Mexico: integration of observations from the seafloor, near-surface, and deep subsurface: GCSSEPM Foundation 20th Annual Research Conference, Deep-Water Reservoirs of the World, p. 1059-1086.

Wu, N., C. A. Jackson, H. Johnson, and D. M. Hodgson, 2019, Lithological, petrophysical and seal properties of mass-transport complexes (MTCs), northern Gulf of Mexico: EarthArXiv. February, v. 19.

Figure 1

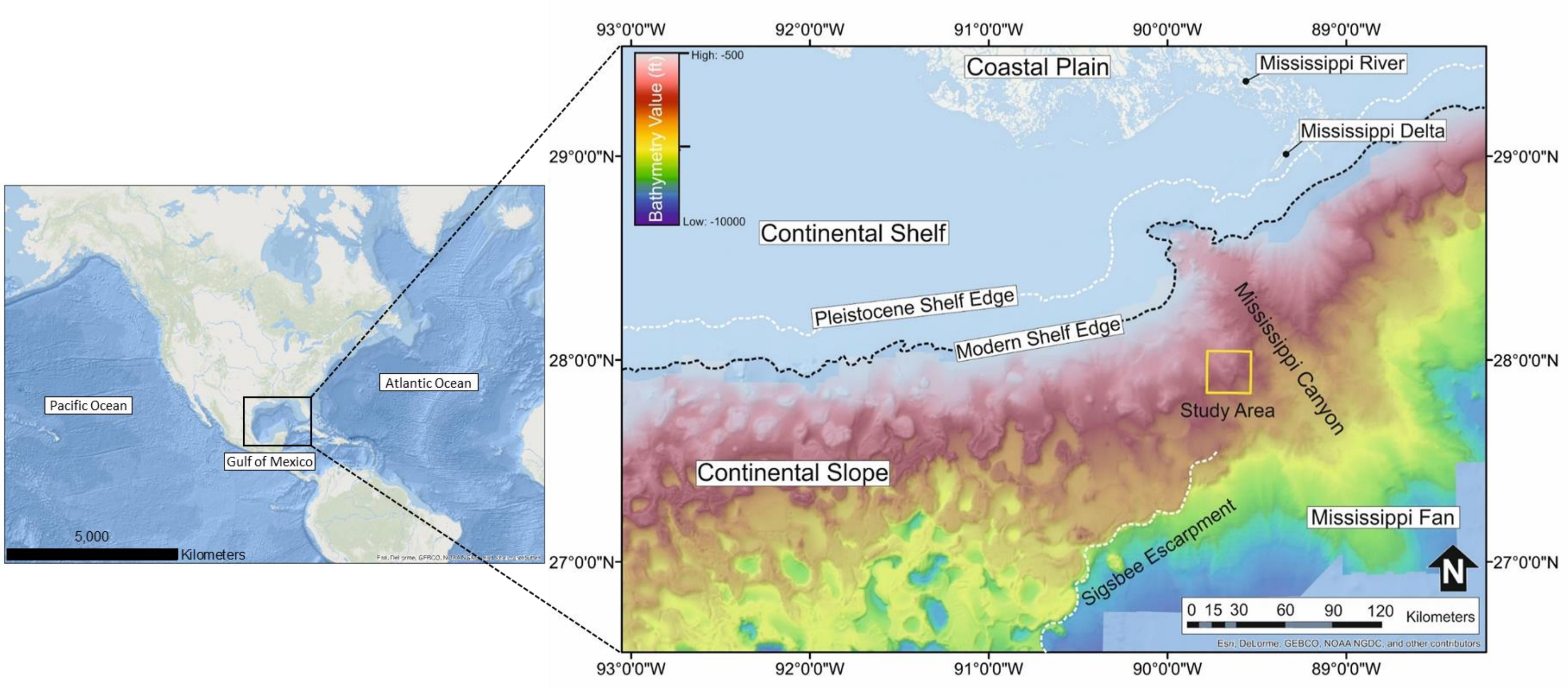

Pacific Ocean
Atlantic Ocean
Gulf of Mexico
5,000
Kilometers
93°0'0"W
92°0'0"W
91°0'0"W
90°0'0"W
89°0'0"W
29°0'0"N
28°0'0"N
27°0'0"N
High: -500
Low: -10000
Bathymetry Value (ft)
Coastal Plain
Mississippi River
Mississippi Delta
Continental Shelf
Pleistocene Shelf Edge
Modern Shelf Edge
Mississippi Canyon
Study Area
Continental Slope
Sigsbee Escarpment
Mississippi Fan
N
0 15 30 60 90 120
Kilometers
Esri, DeLorme, GEBCO, NOAA NGDC, and other contributors

Figure 2

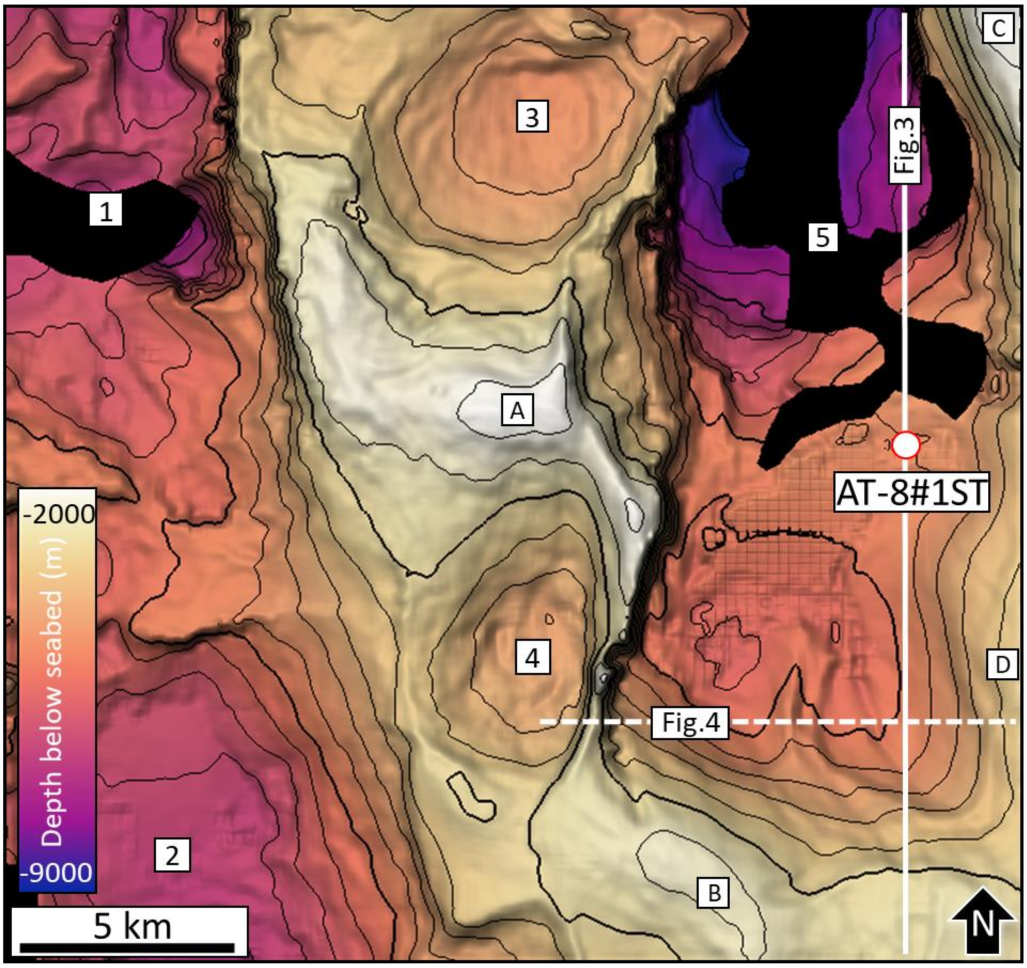

C
3
Fig.3
1
5
A
AT-8#1ST
-2000
Depth below seabed (m)
-9000
4
D
Fig.4
2
B
5 km
N

Figure 3a

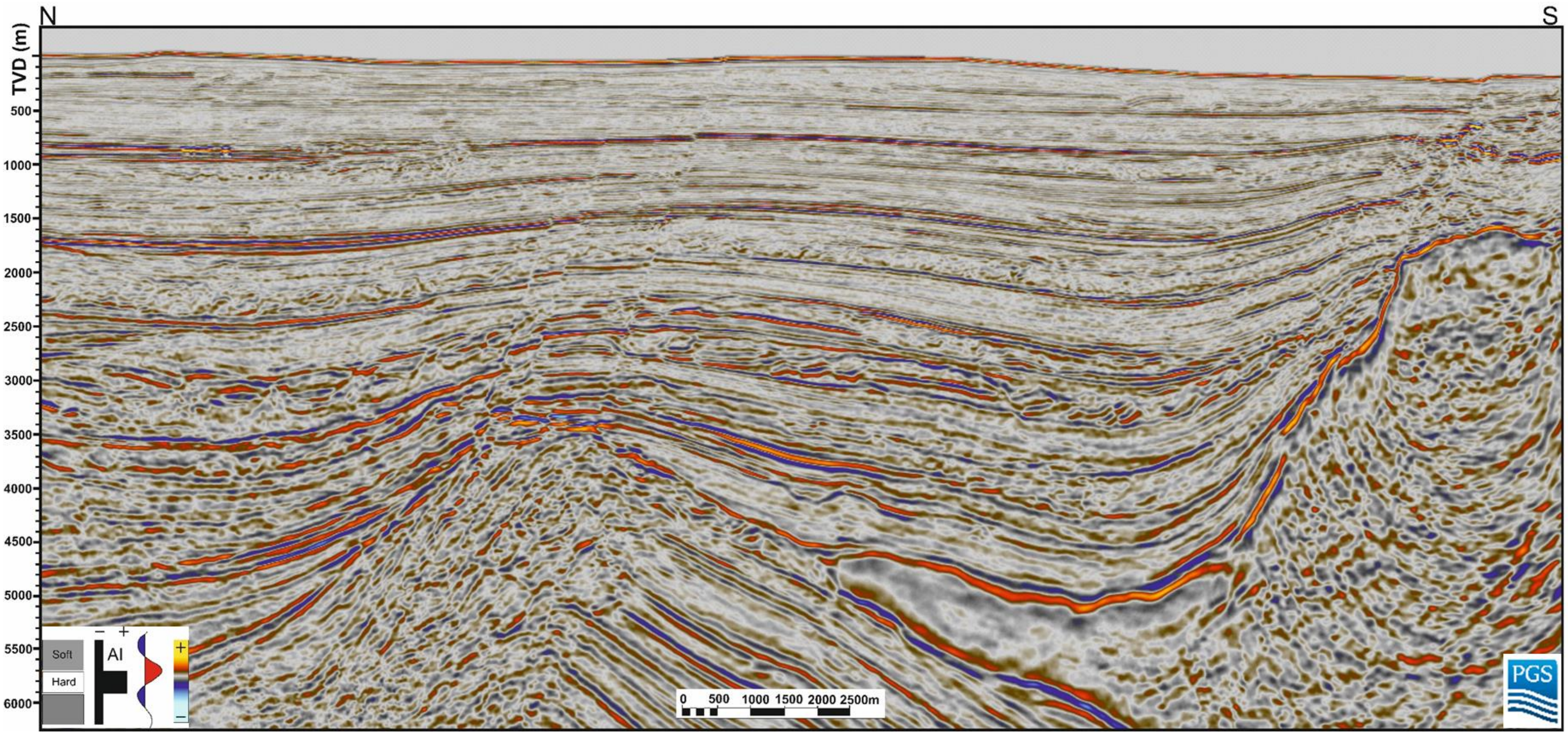
N
S
TVD (m)
500
1000
1500
2000
2500
3000
3500
4000
4500
5000
5500
6000
Soft
Hard
AI
0 500 1000 1500 2000 2500m
PGS

Figure 3b

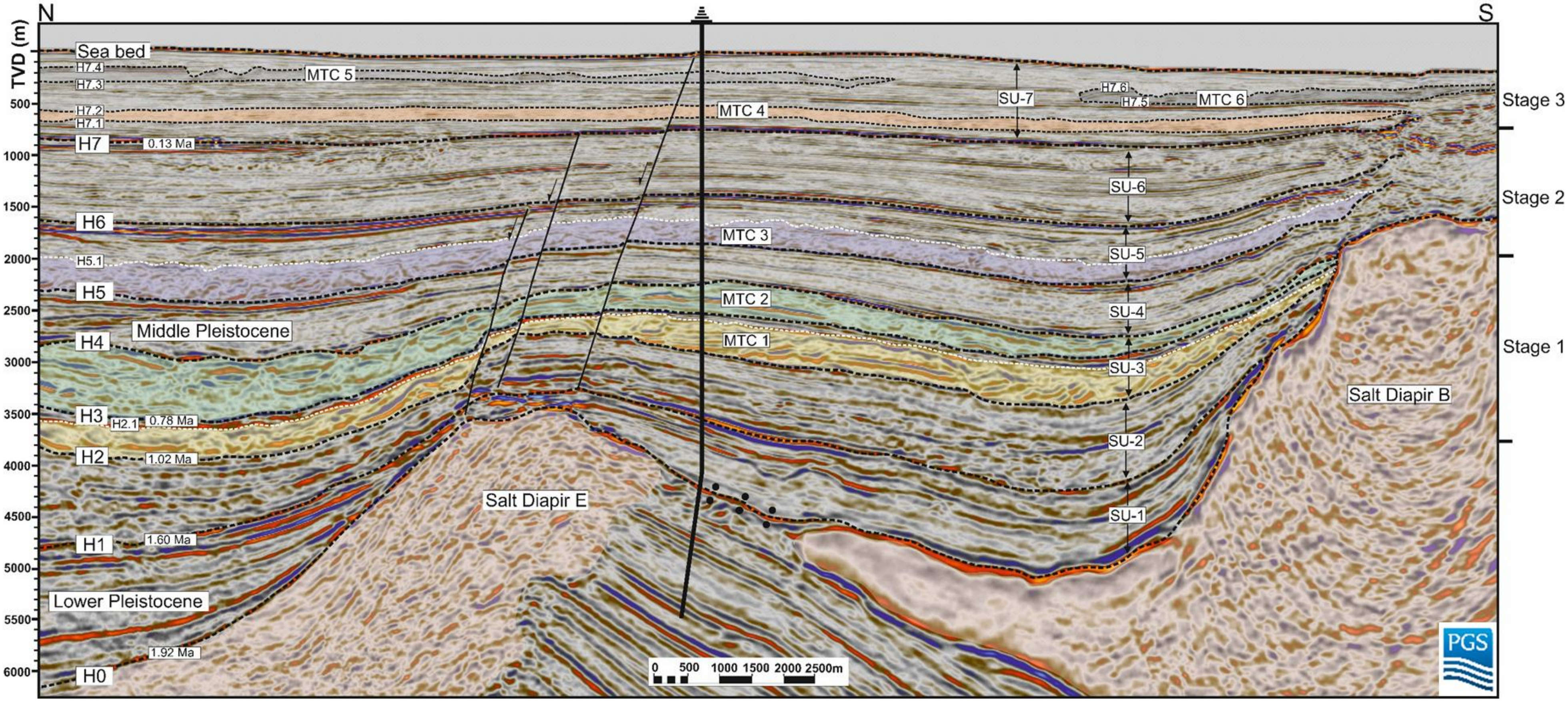

N
S
TVD (m)
Sea bed
H7.4
H7.3
H7.2
H7.1
H7
0.13 Ma
MTC 5
MTC 4
SU-7
H7.6
H7.5
MTC 6
Stage 3
SU-6
Stage 2
H6
MTC 3
H5.1
SU-5
H5
MTC 2
SU-4
Middle Pleistocene
H4
MTC 1
Stage 1
SU-3
H3
H2.1
0.78 Ma
H2
1.02 Ma
SU-2
Salt Diapir B
Salt Diapir E
SU-1
H1
1.60 Ma
Lower Pleistocene
1.92 Ma
H0
0 500 1000 1500 2000 2500m

Figure 4a

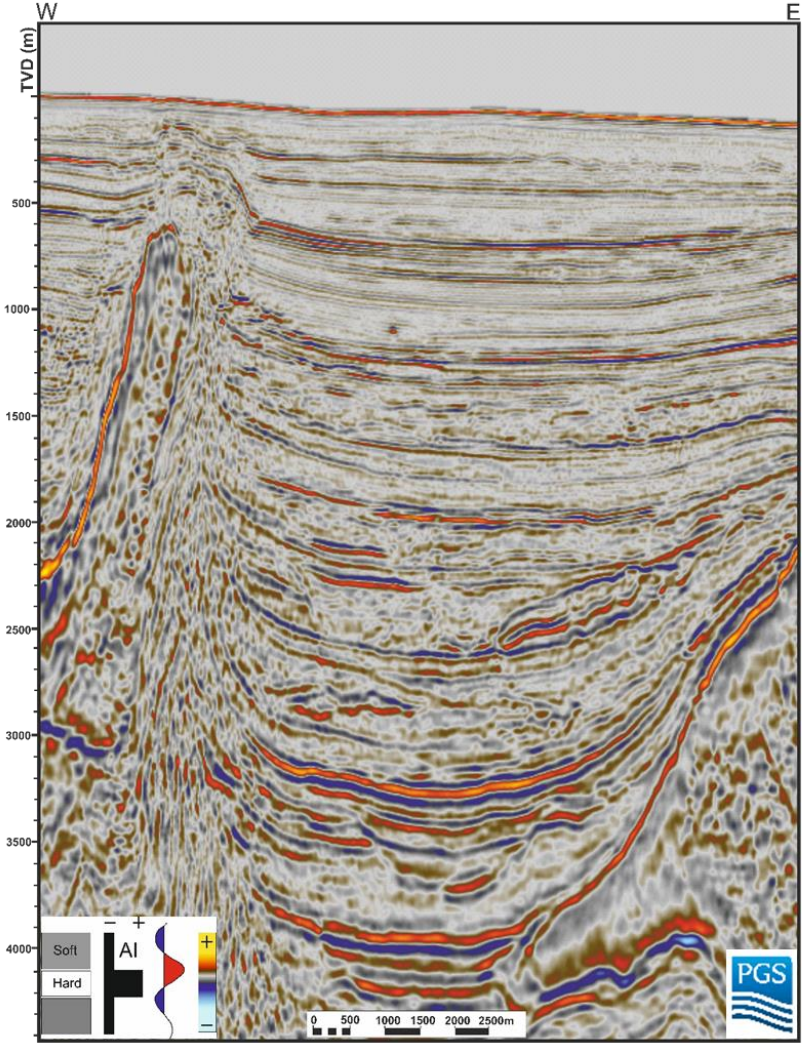

Figure 4b

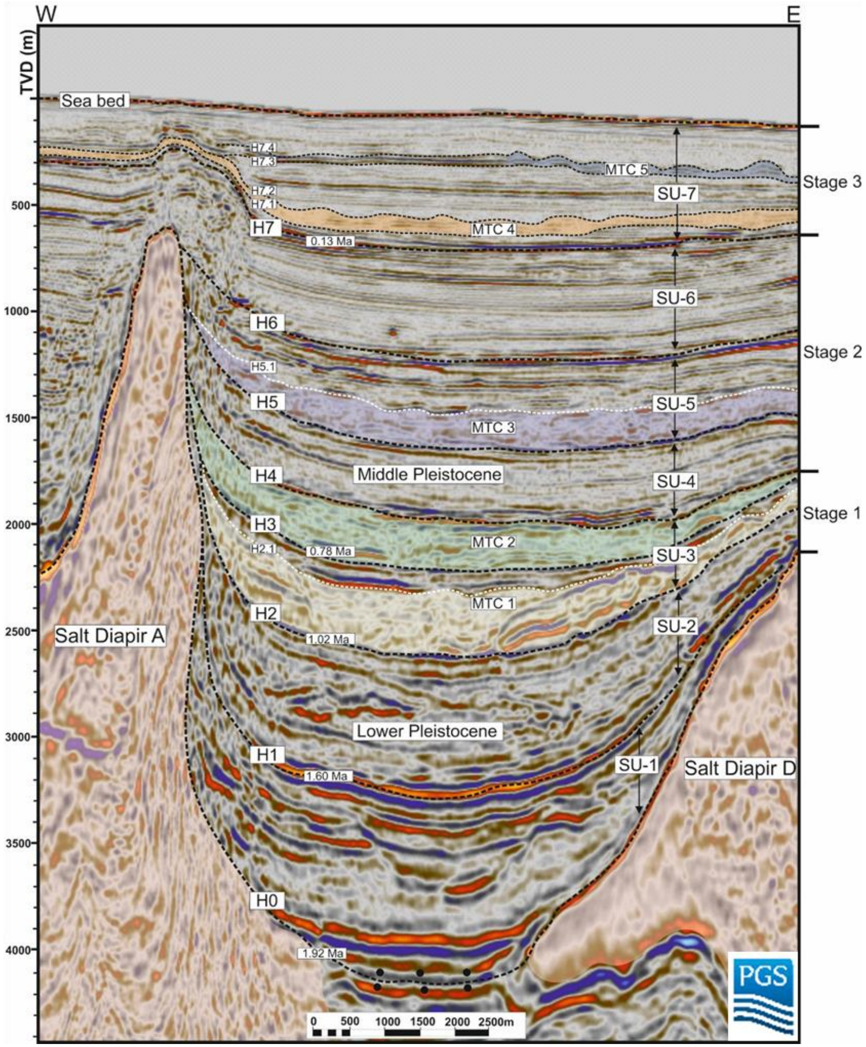

Figure 5

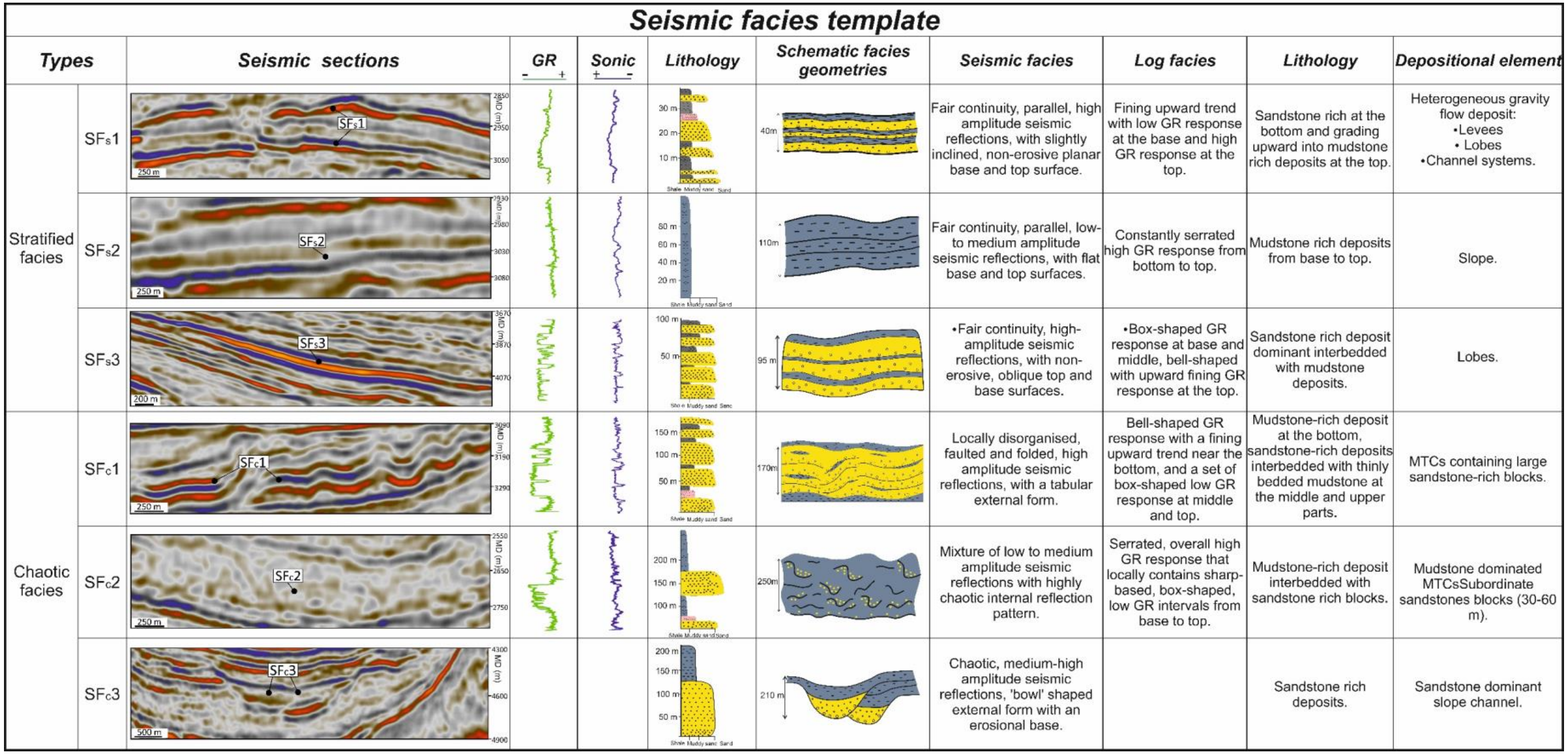
Seismic facies template
Types
Seismic sections
GR
Sonic
Lithology
Schematic facies geometries
Seismic facies
Log facies
Lithology
Depositional element
Stratified facies
SFs1
Fair continuity, parallel, high amplitude seismic reflections, with slightly inclined, non-erosive planar base and top surface.
Fining upward trend with low GR response at the base and high GR response at the top.
Sandstone rich at the bottom and grading upward into mudstone rich deposits at the top.
Heterogeneous gravity flow deposit: •Levees • Lobes •Channel systems.
SFs2
Fair continuity, parallel, low- to medium amplitude seismic reflections, with flat base and top surfaces.
Constantly serrated high GR response from bottom to top.
Mudstone rich deposits from base to top.
Slope.
SFs3
•Fair continuity, high-amplitude seismic reflections, with non-erosive, oblique top and base surfaces.
•Box-shaped GR response at base and middle, bell-shaped with upward fining GR response at the top.
Sandstone rich deposit dominant interbedded with mudstone deposits.
Lobes.
Chaotic facies
SFc1
Locally disorganised, faulted and folded, high amplitude seismic reflections, with a tabular external form.
Bell-shaped GR response with a fining upward trend near the bottom, and a set of box-shaped low GR response at middle and top.
Mudstone-rich deposit at the bottom, sandstone-rich deposits interbedded with thinly bedded mudstone at the middle and upper parts.
MTCs containing large sandstone-rich blocks.
SFc2
Mixture of low to medium amplitude seismic reflections with highly chaotic internal reflection pattern.
Serrated, overall high GR response that locally contains sharp-based, box-shaped, low GR intervals from base to top.
Mudstone-rich deposit interbedded with sandstone rich blocks.
Mudstone dominated MTCsSubordinate sandstones blocks (30-60 m).
SFc3
Chaotic, medium-high amplitude seismic reflections, 'bowl' shaped external form with an erosional base.
Sandstone rich deposits.
Sandstone dominant slope channel.

Figure 6

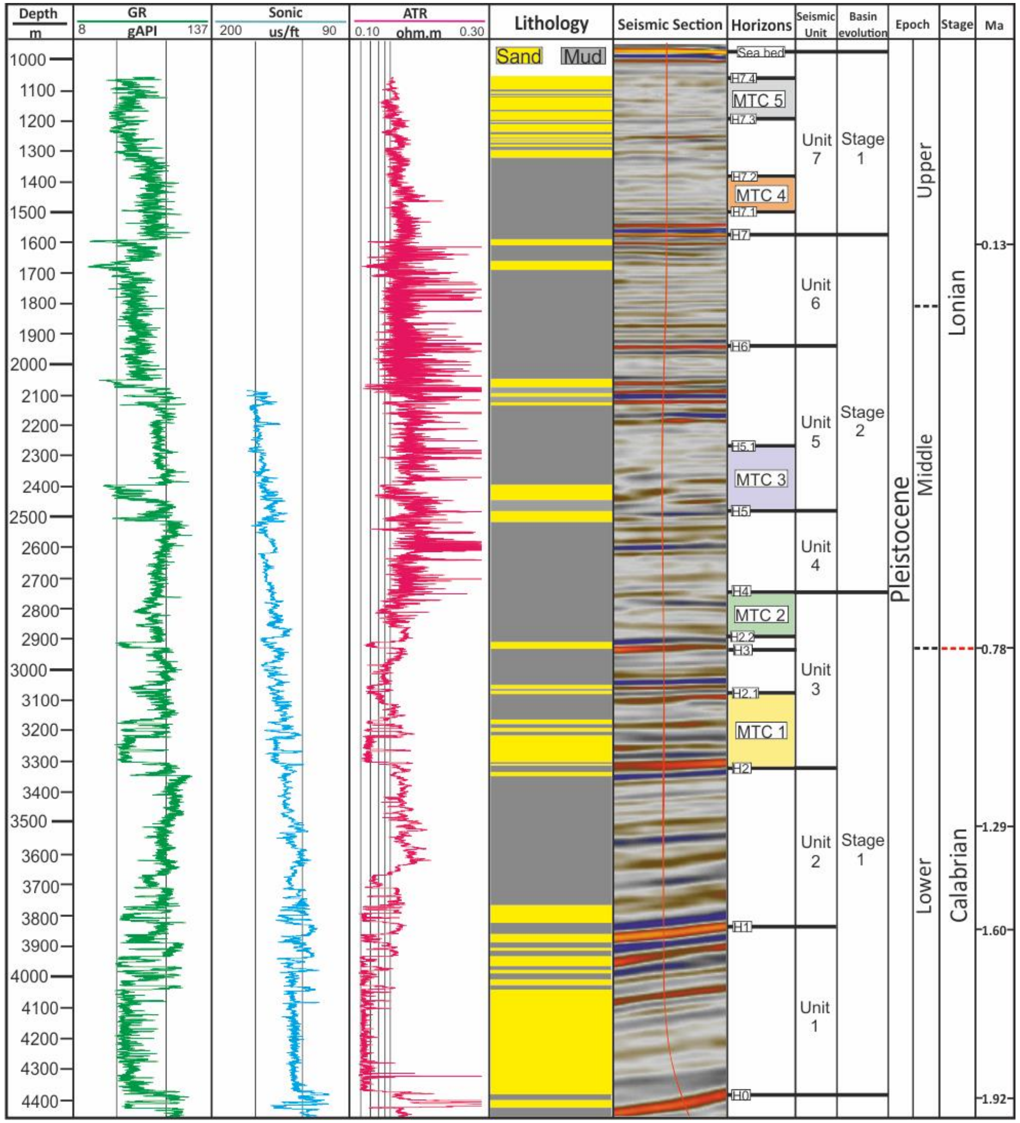

Depth
m
GR
8 gAPI 137
Sonic
200 us/ft 90
ATR
0.10 ohm.m 0.30
Lithology
Sand
Mud
Seismic Section
Horizons
Seismic Unit
Basin evolution
Epoch
Stage
Ma
1000
1100
1200
1300
1400
1500
1600
1700
1800
1900
2000
2100
2200
2300
2400
2500
2600
2700
2800
2900
3000
3100
3200
3300
3400
3500
3600
3700
3800
3900
4000
4100
4200
4300
4400
Sea bed
H7.4
MTC 5
H7.3
H7.2
MTC 4
H7.1
H7
H6
H5.1
MTC 3
H5
H4
MTC 2
H2.2
H3
H2.1
MTC 1
H2
H1
H0
Unit 7
Unit 6
Unit 5
Unit 4
Unit 3
Unit 2
Unit 1
Stage 1
Stage 2
Stage 1
Pleistocene
Upper
Middle
Lower
Lonian
Calabrian
0.13
0.78
1.29
1.60
1.92

Figure 7a

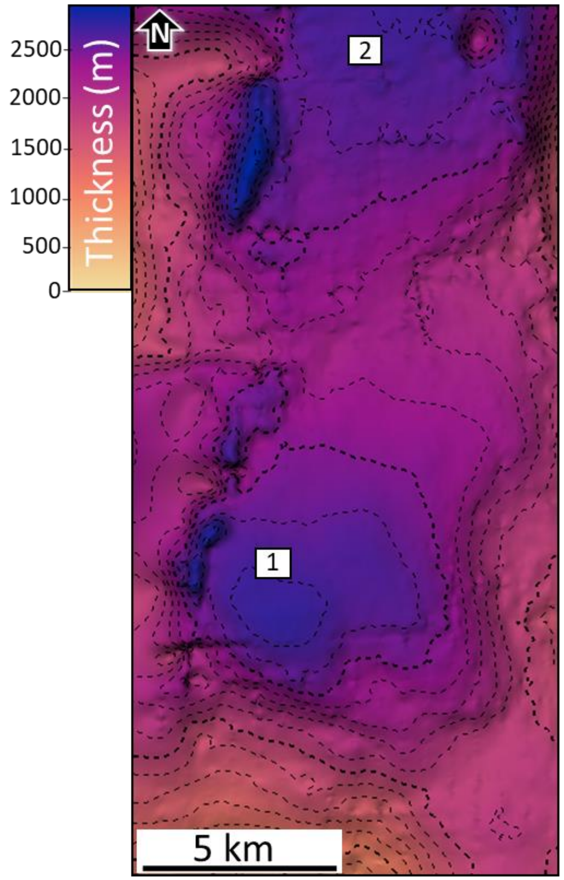

Figure 7b

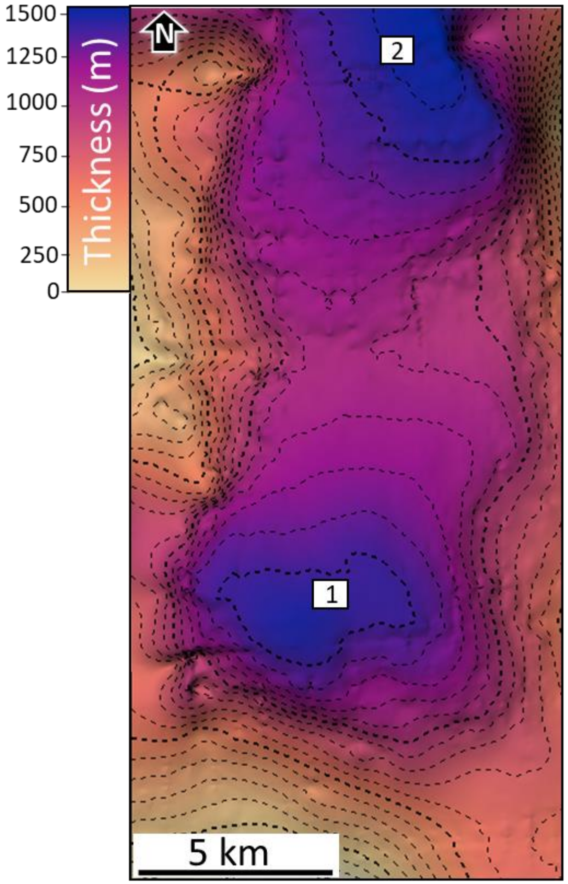

Figure 7c

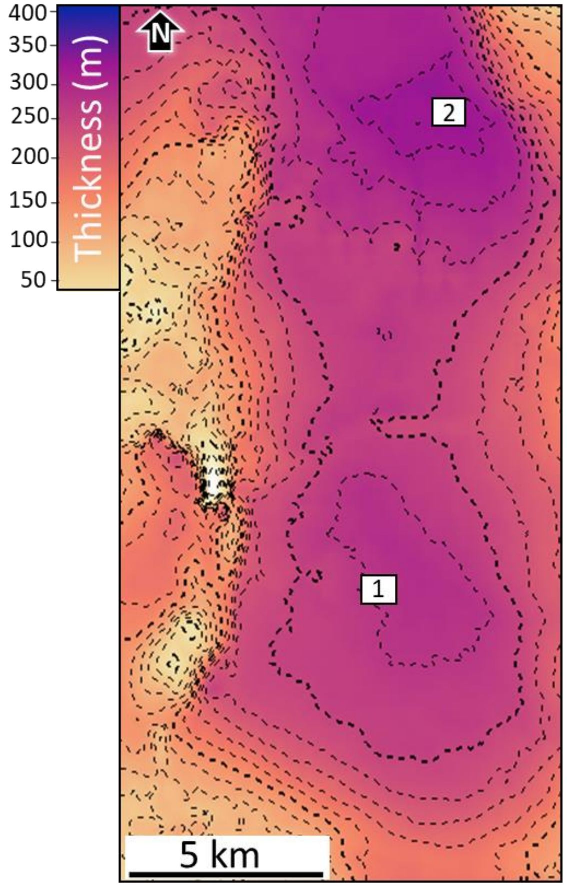

Figure 8a

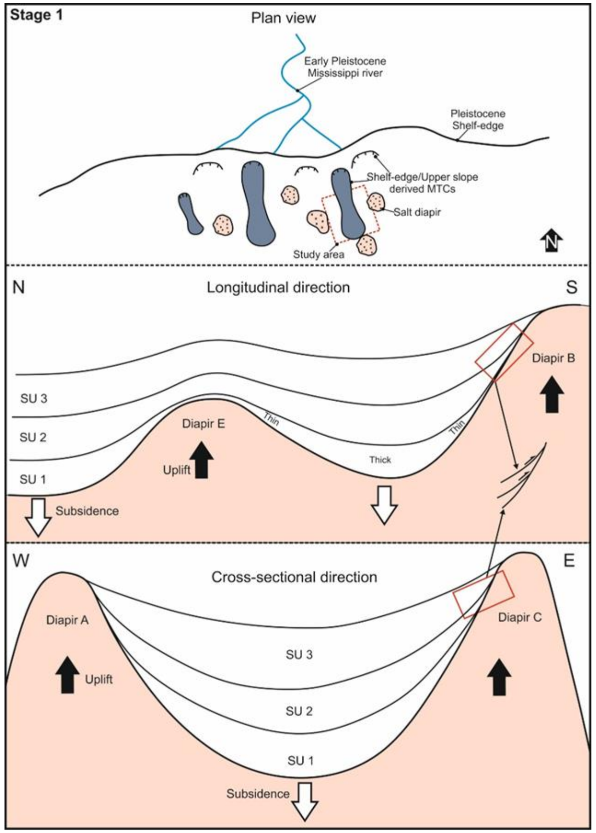

Figure 8b

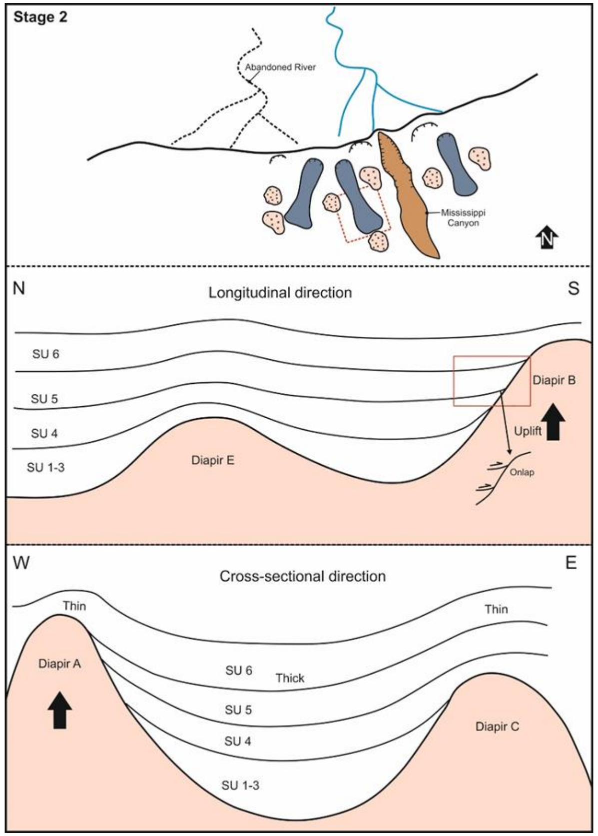

Figure 8c

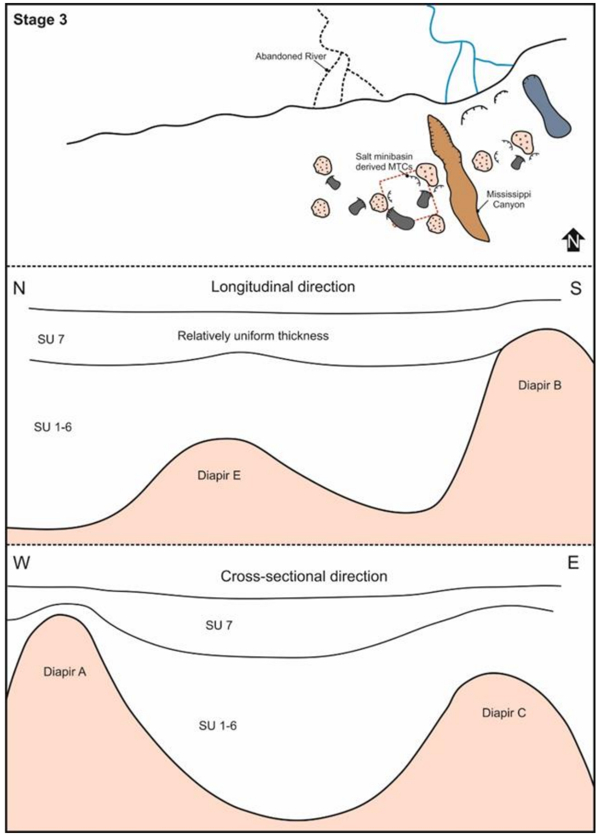

Figure 9

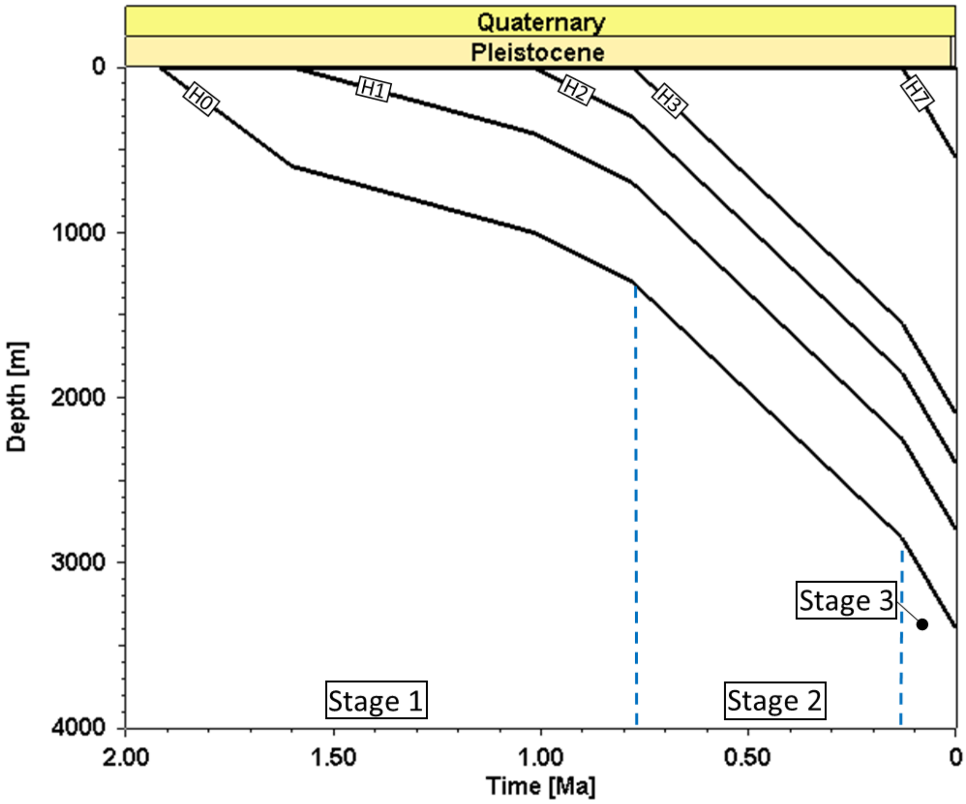
Quaternary
Pleistocene
H0
H1
H2
H3
H7
Stage 1
Stage 2
Stage 3
Depth [m]
0
1000
2000
3000
4000
2.00
1.50
1.00
0.50
0
Time [Ma]

Figure 10a

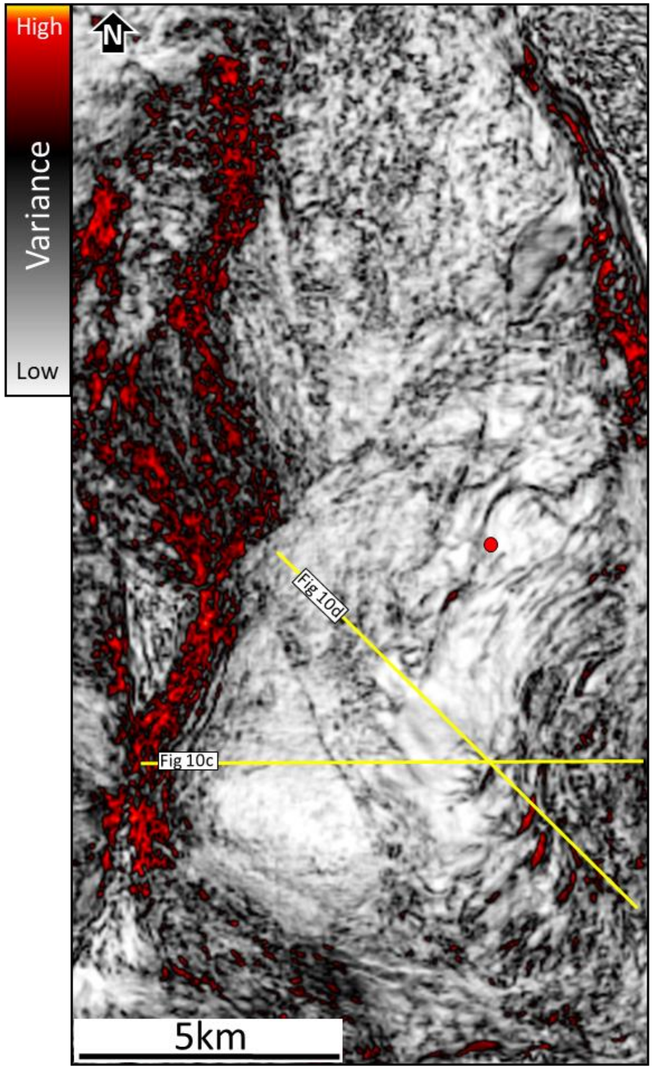

Figure 10b

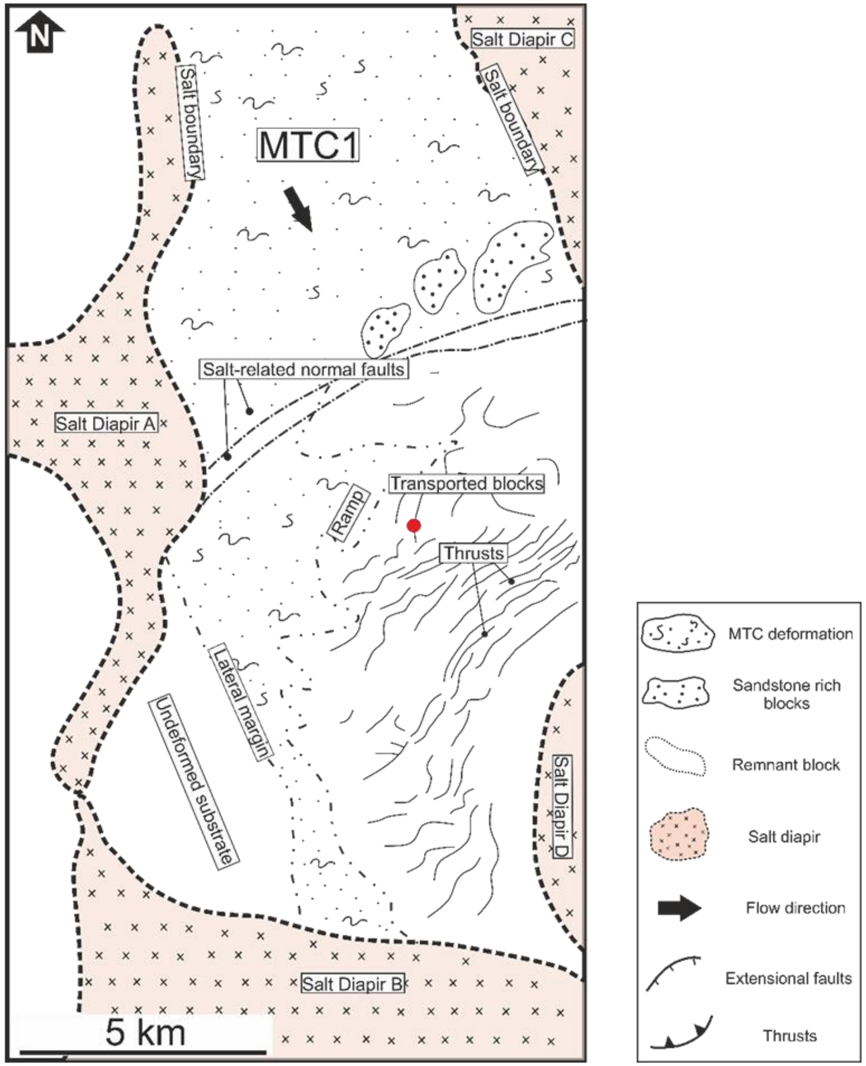

Figure 10c

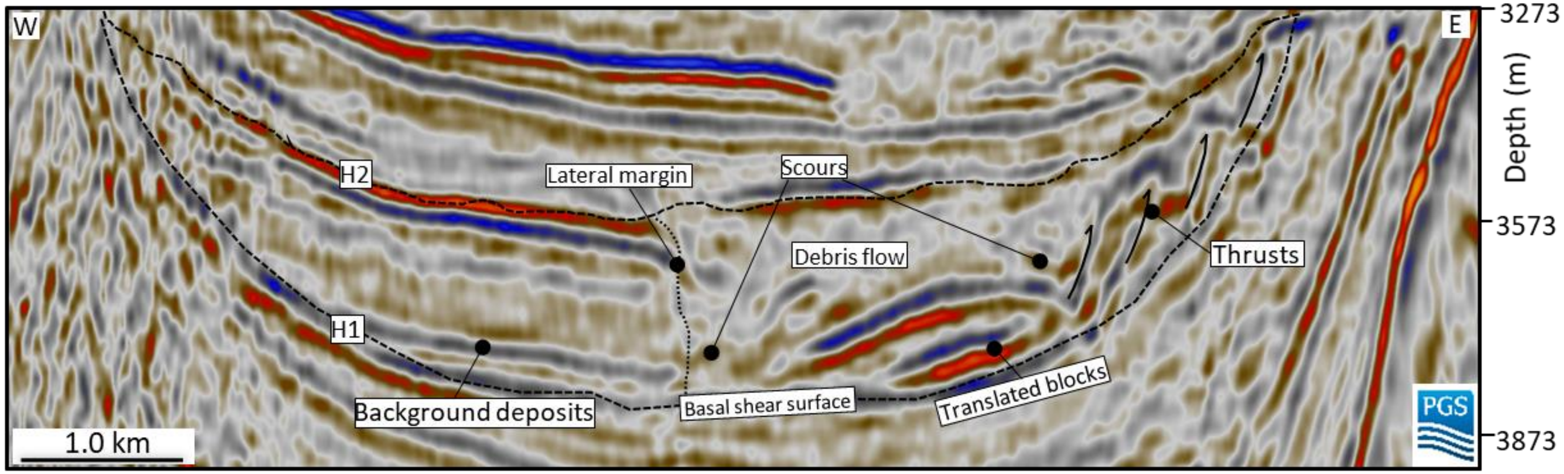

Figure 10d

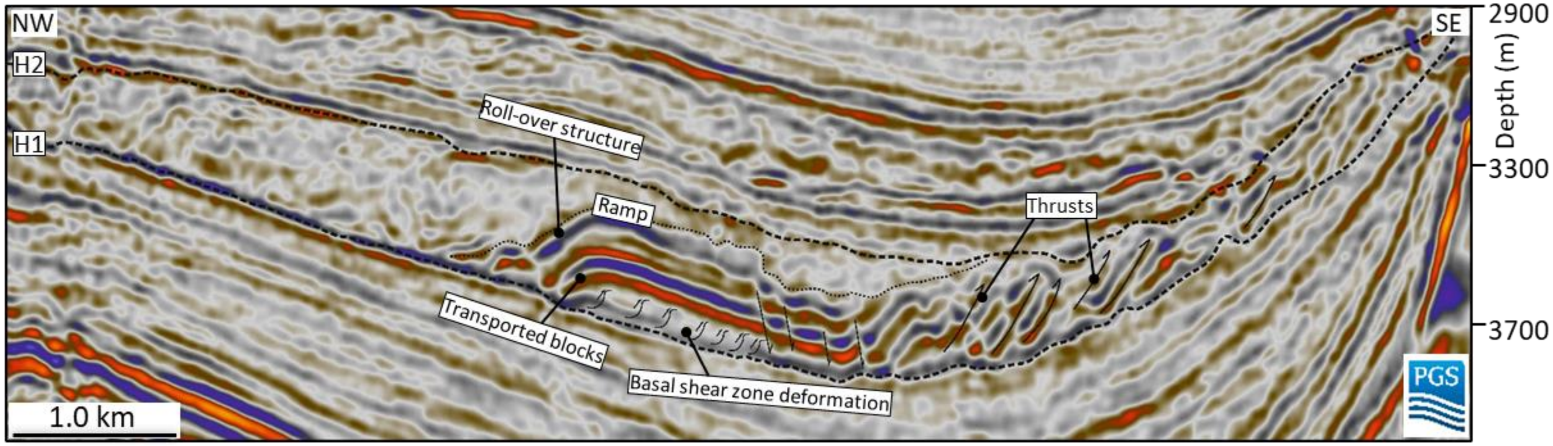

Figure 11a

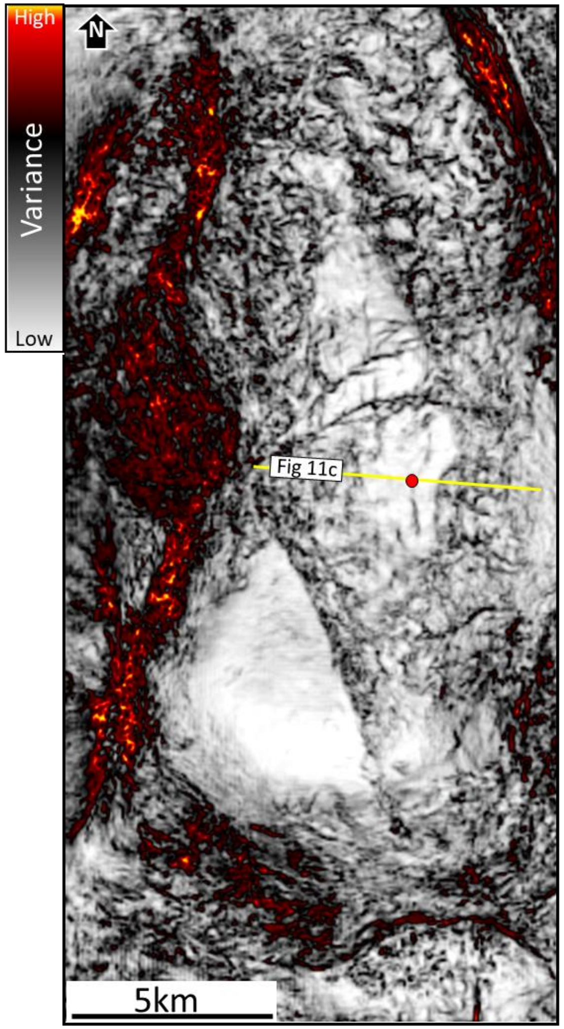

Figure 11b

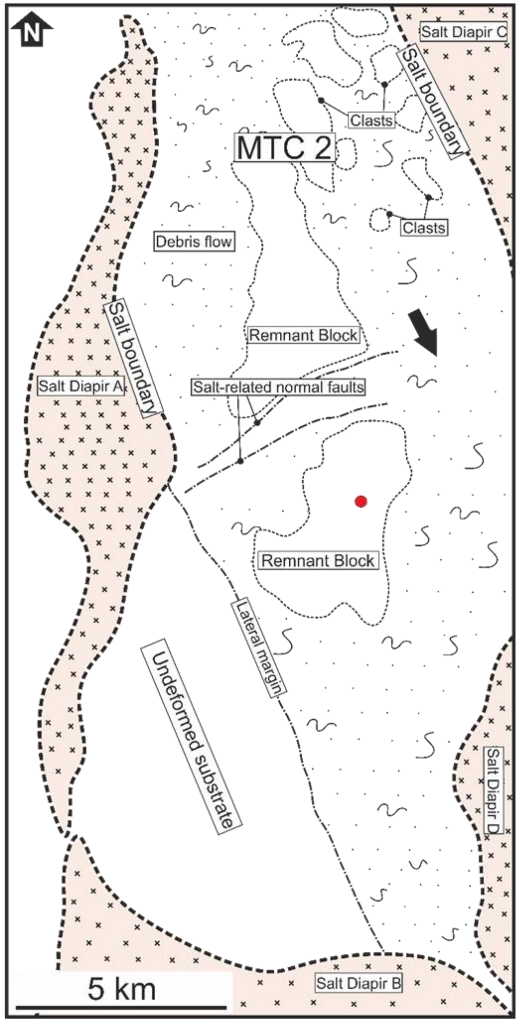

Figure 11c

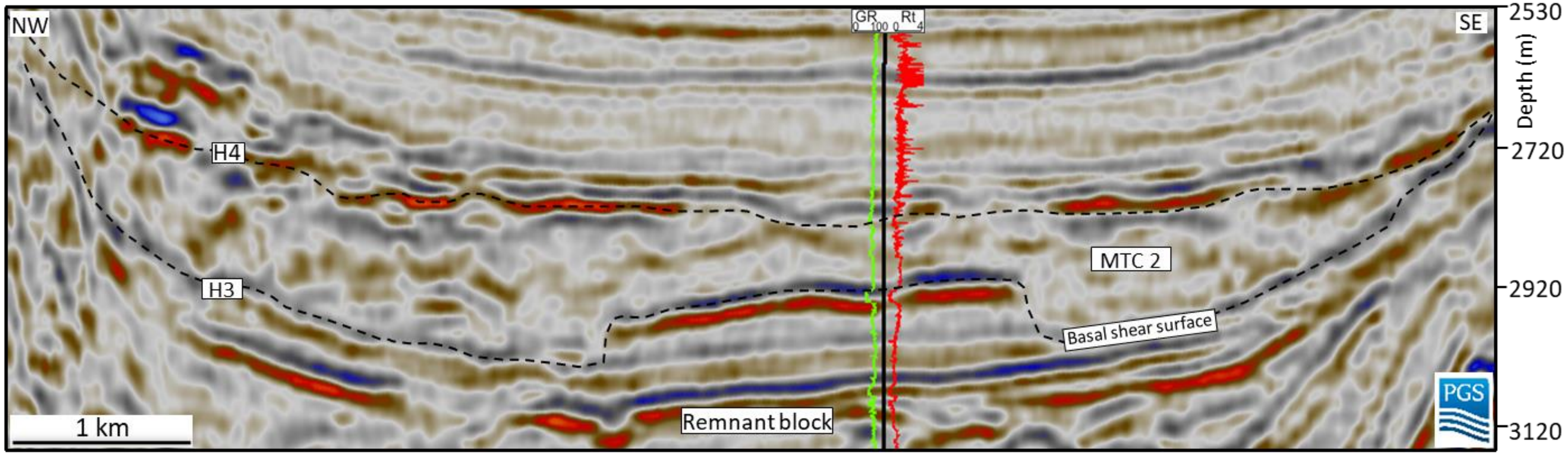
NW
SE
GR
0 100
Rt
0 4
H4
H3
MTC 2
Basal shear surface
Remnant block
1 km
PGS
2530
2720
2920
3120
Depth (m)

Figure 12a

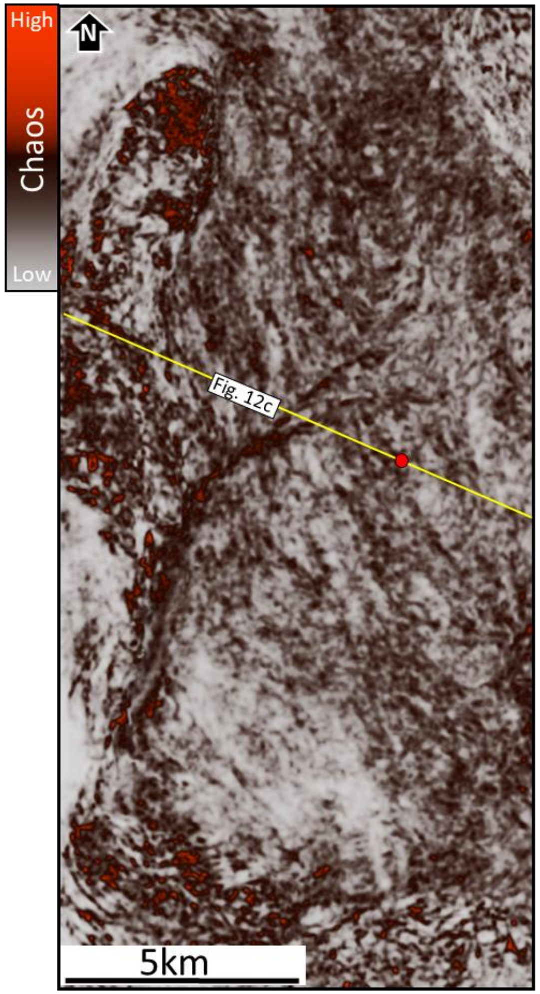

Figure 12b

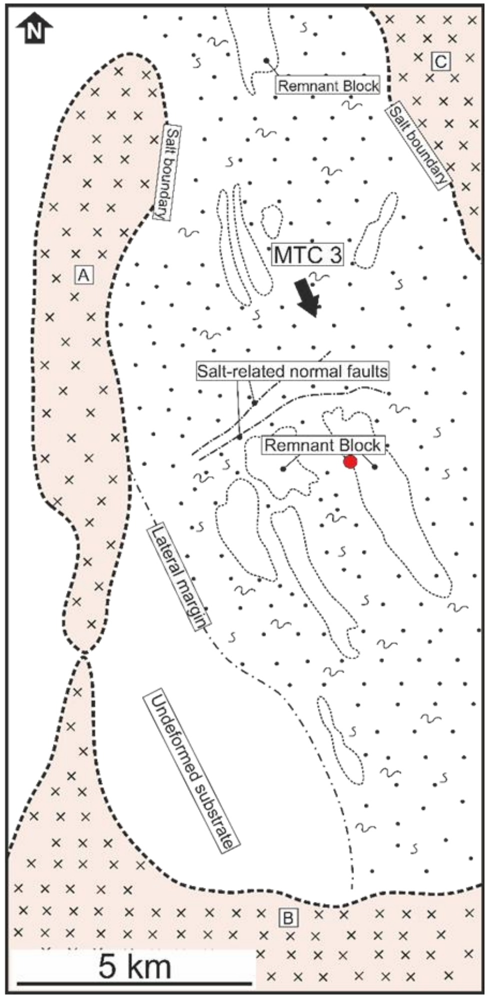

Figure 12c

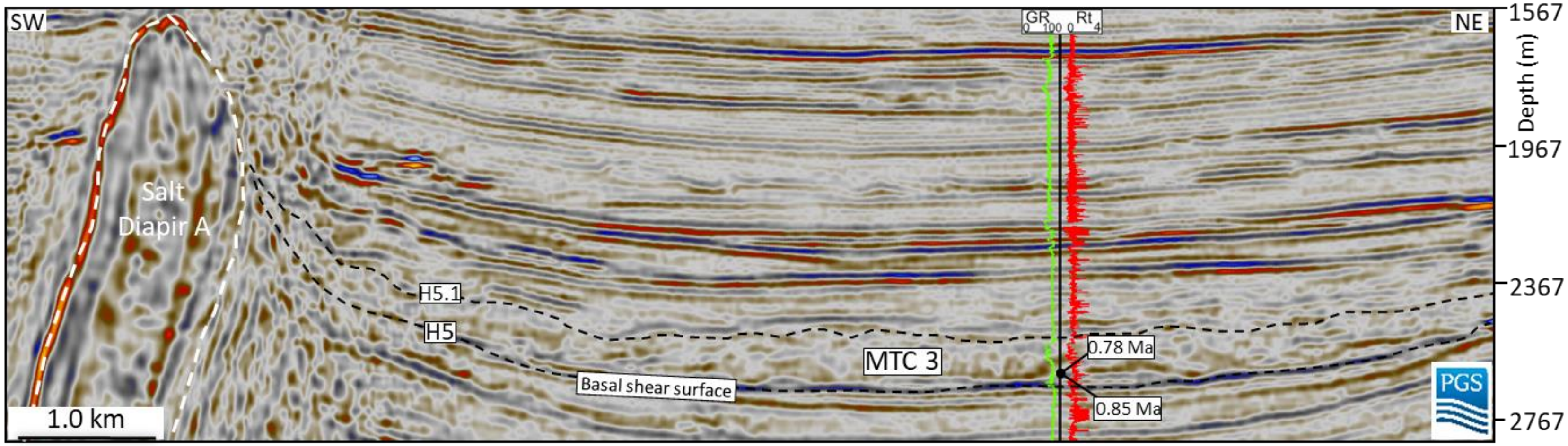

SW
NE
GR
0 100
Rt
0 4
1567
Depth (m)
1967
2367
2767
Salt
Diapir A
H5.1
H5
MTC 3
0.78 Ma
0.85 Ma
Basal shear surface
PGS
1.0 km

Figure 12d

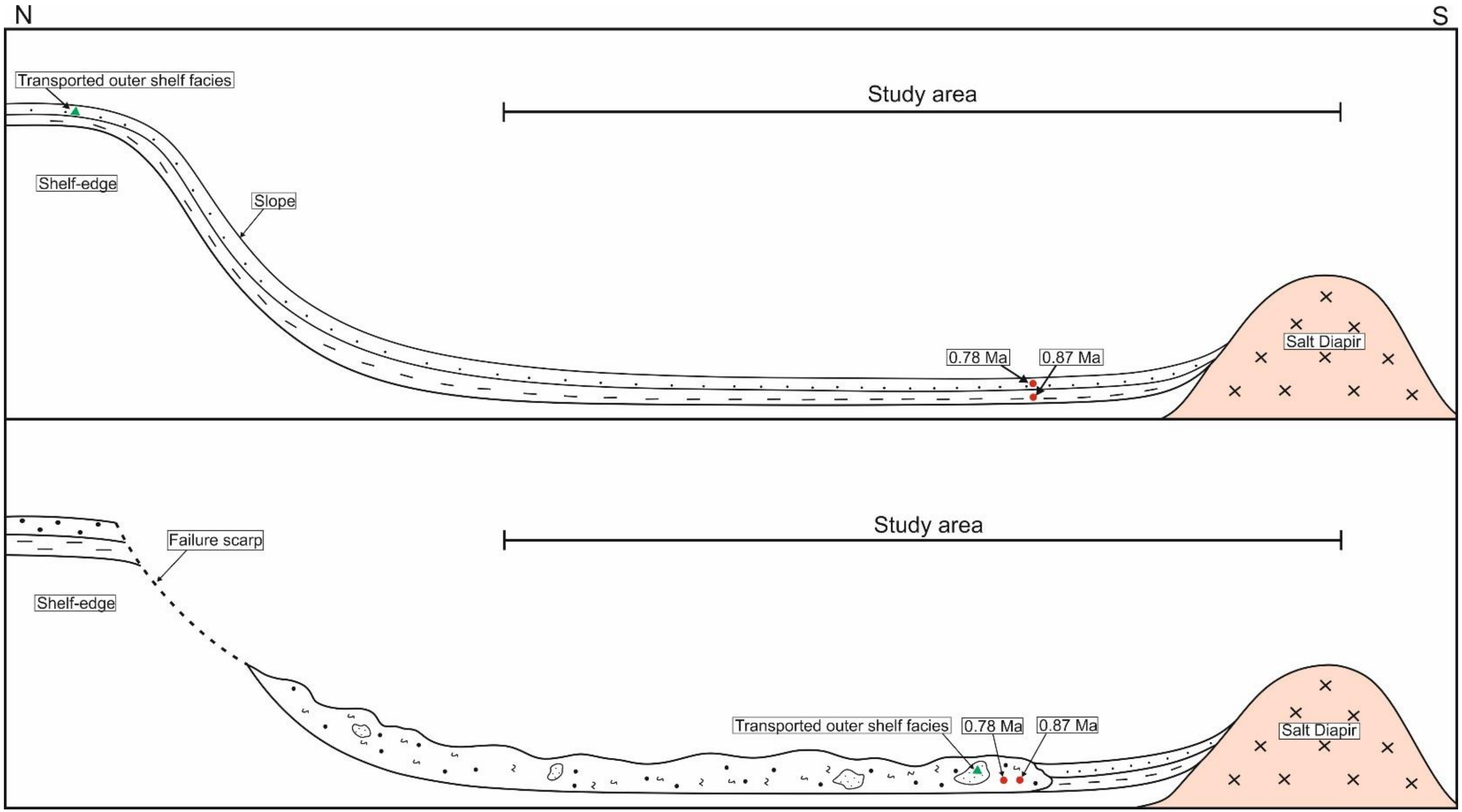
N
S
Transported outer shelf facies
Study area
Shelf-edge
Slope
Salt Diapir
0.78 Ma
0.87 Ma
Study area
Failure scarp
Shelf-edge
Transported outer shelf facies
0.78 Ma
0.87 Ma
Salt Diapir

Figure 12e

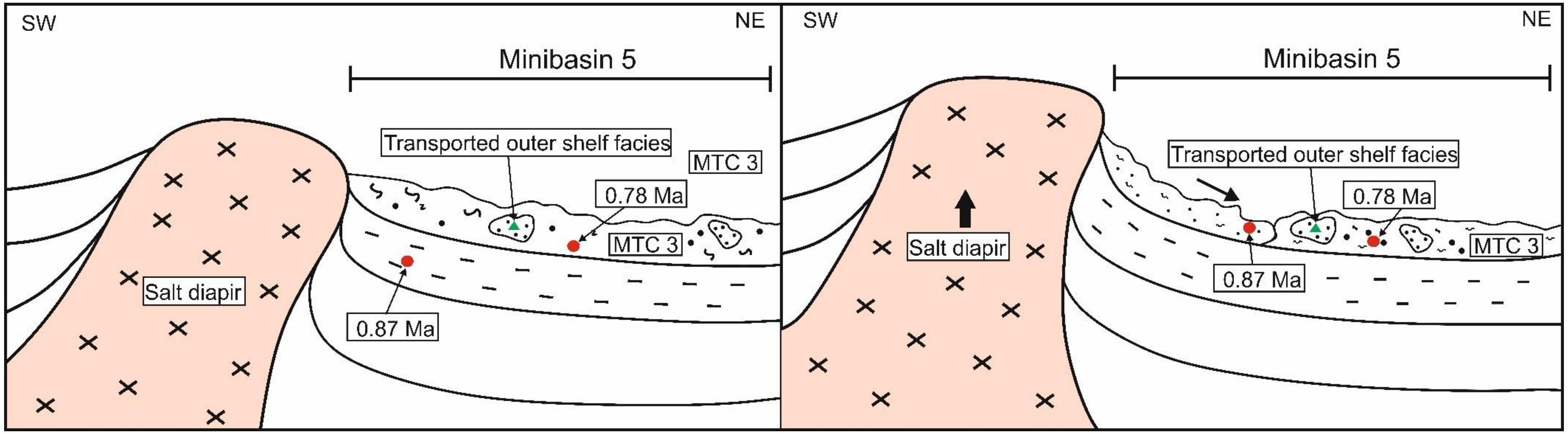

SW
NE
Minibasin 5
Transported outer shelf facies
MTC 3
0.78 Ma
MTC 3
Salt diapir
0.87 Ma
SW
NE
Minibasin 5
Transported outer shelf facies
0.78 Ma
Salt diapir
MTC 3
0.87 Ma

Figure 13

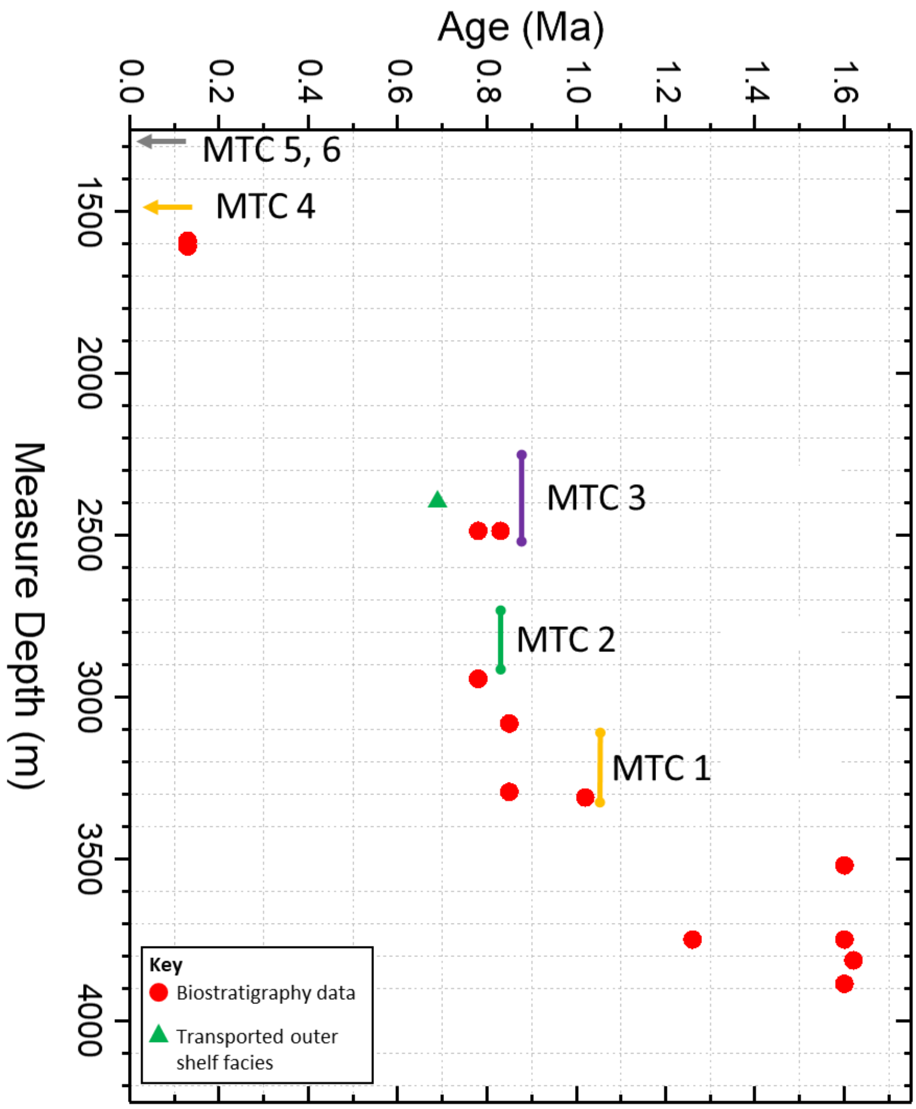

Age (Ma)
0.0
0.2
0.4
0.6
0.8
1.0
1.2
1.4
1.6
Measure Depth (m)
1500
2000
2500
3000
3500
4000
MTC 5, 6
MTC 4
MTC 3
MTC 2
MTC 1
Key
Biostratigraphy data
Transported outer shelf facies

Figure 14a

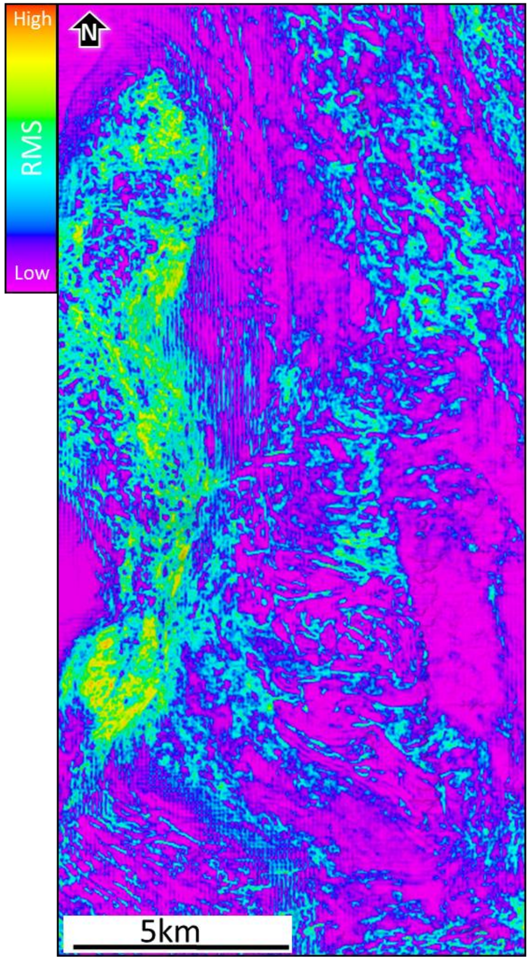

Figure 14b

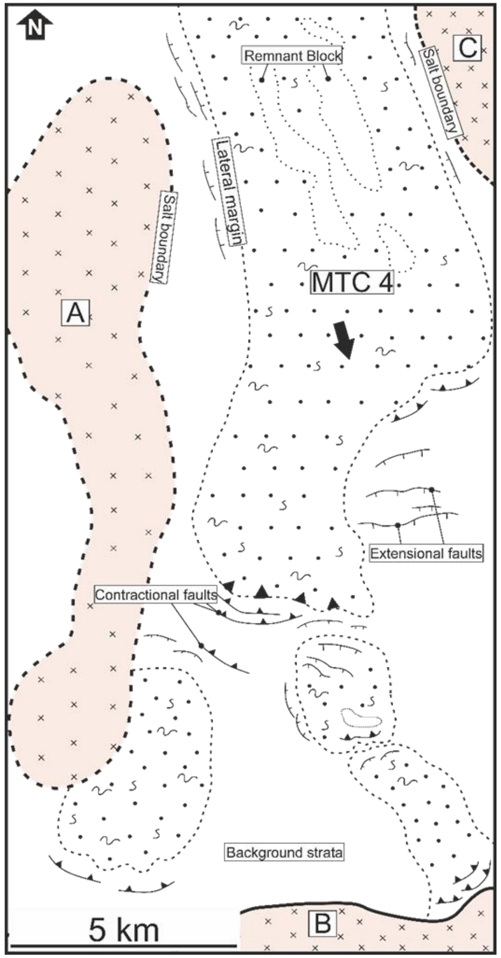

Figure 15a

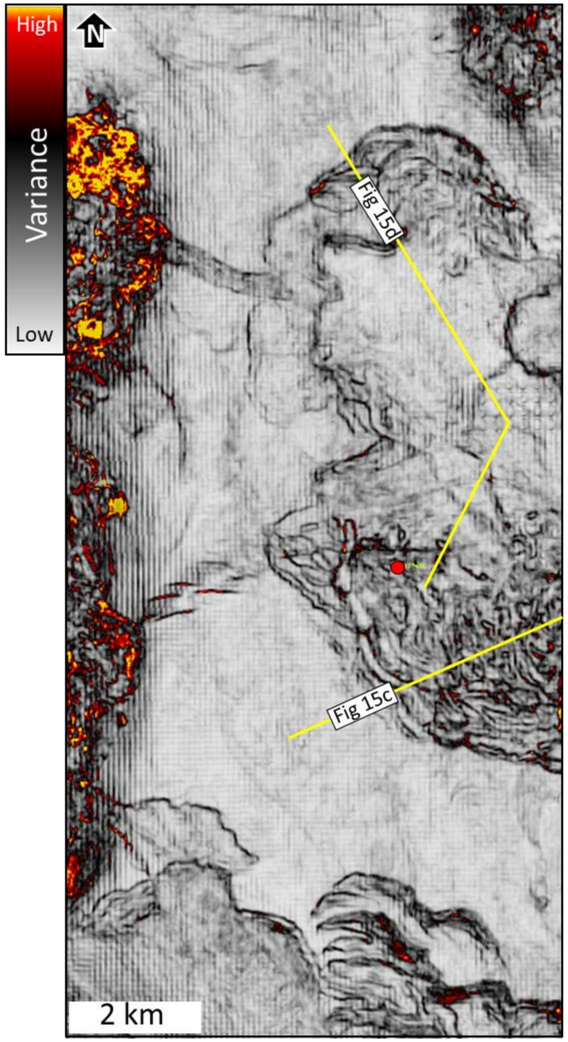

Figure 15b

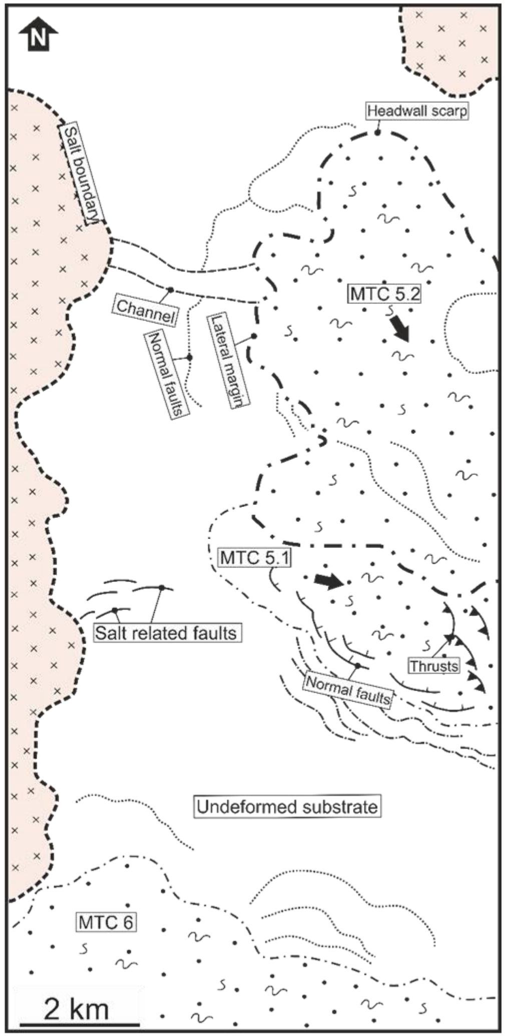

Figure15c

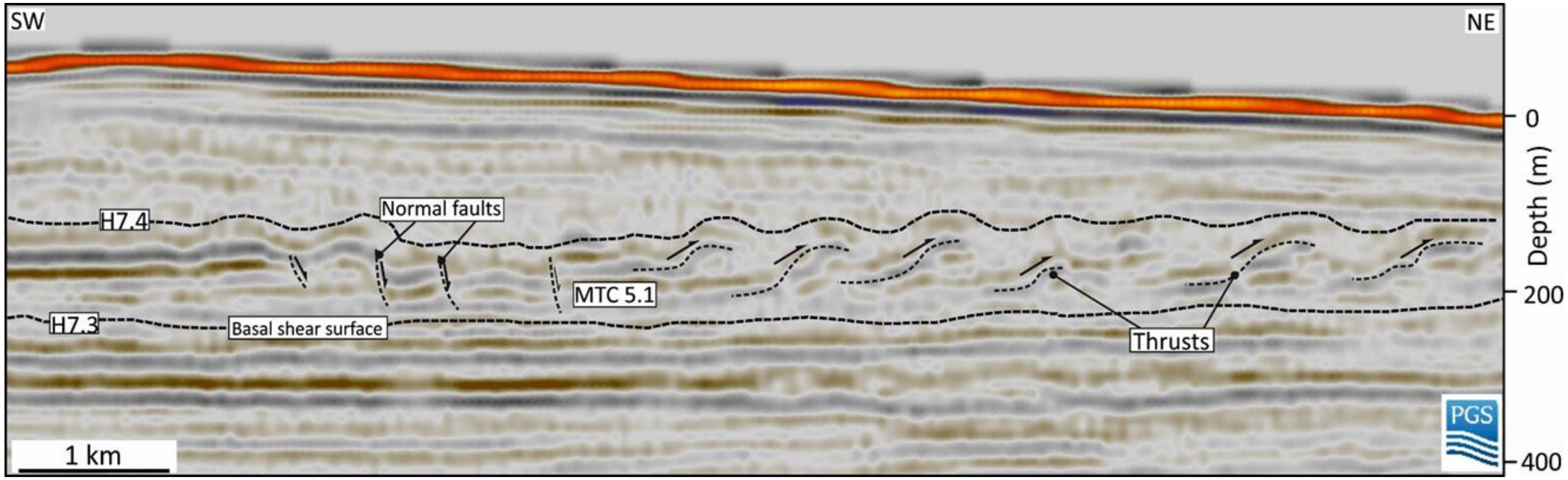

Figure 15d

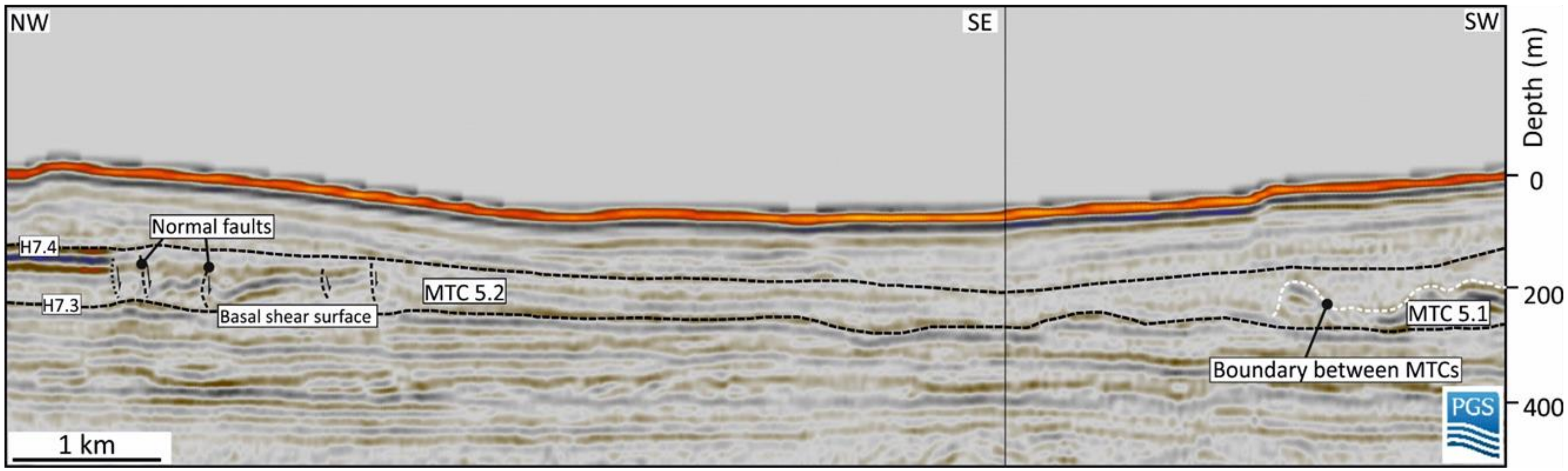

Figure 16a

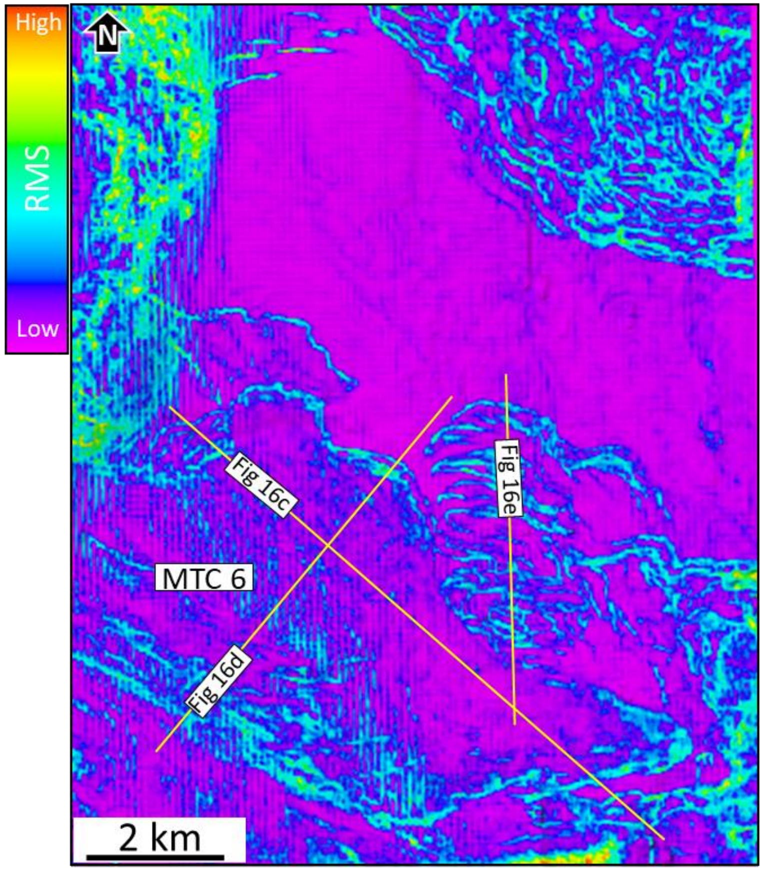

Figure 16b

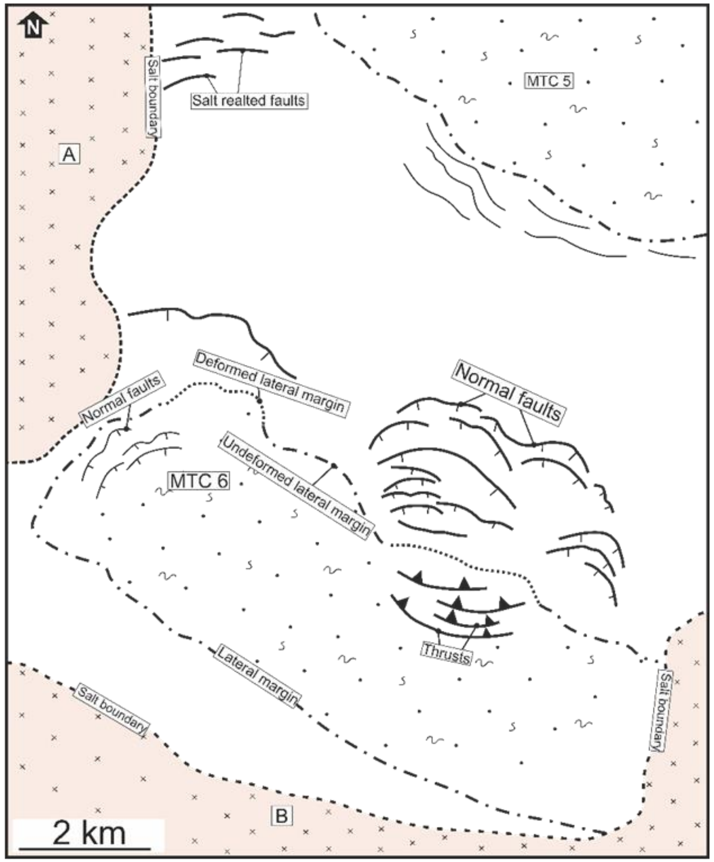

Figure 16c

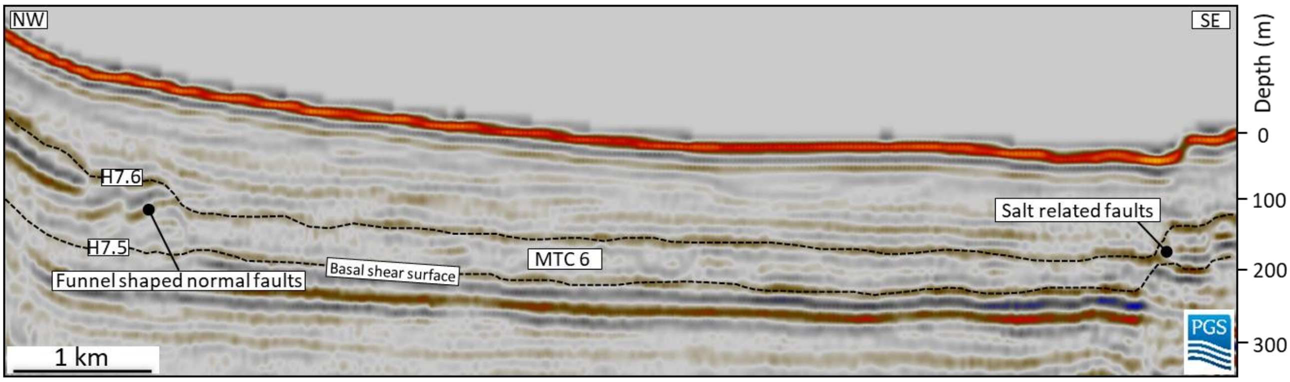

Figure 16d

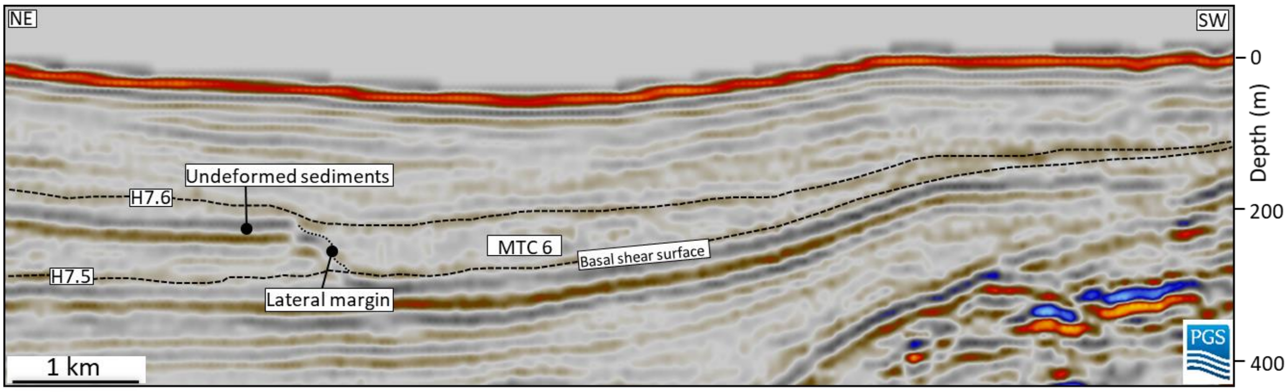

Figure 16e

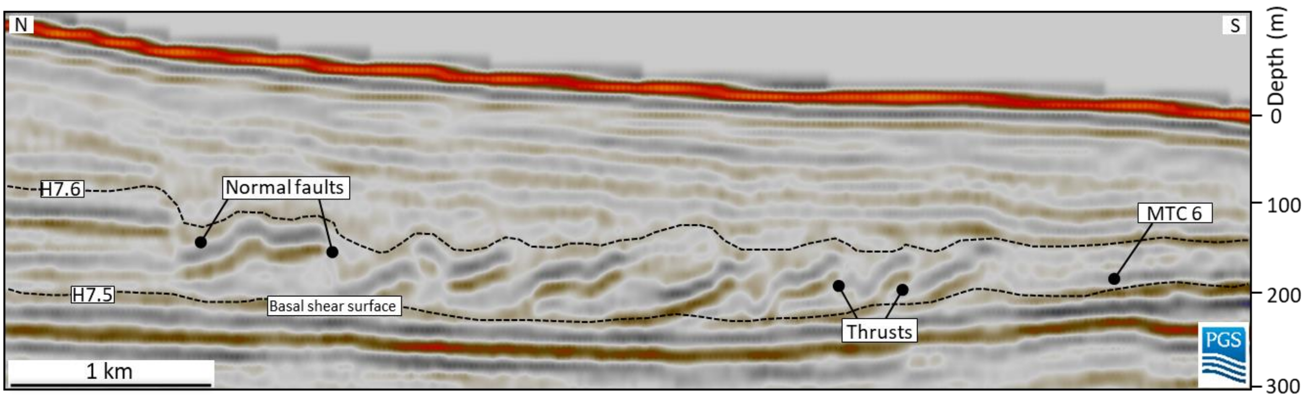

Figure 16f

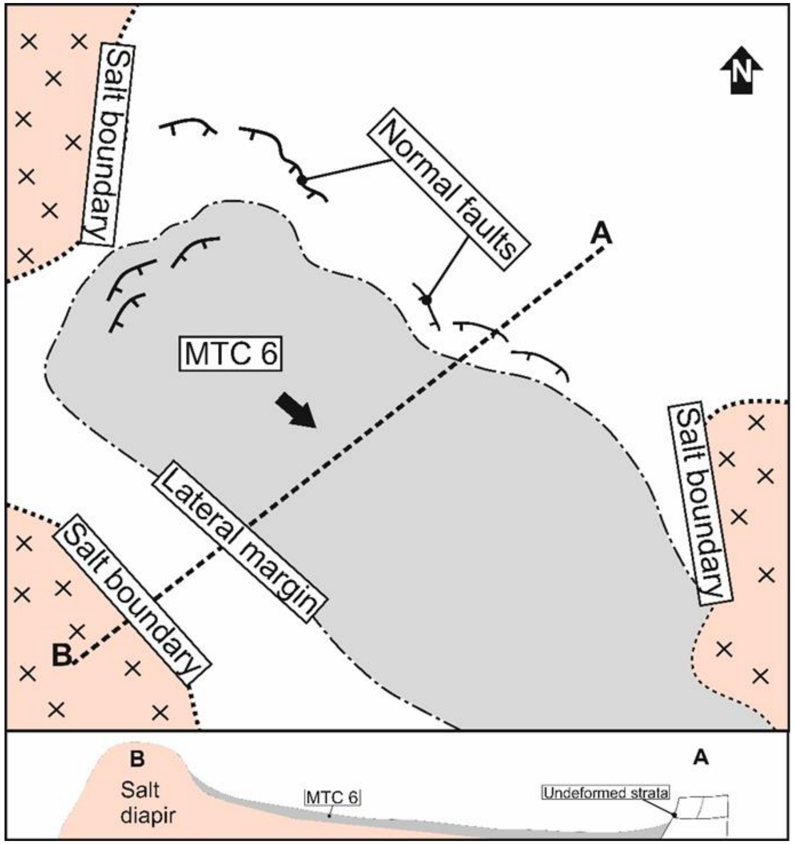

Figure 16g

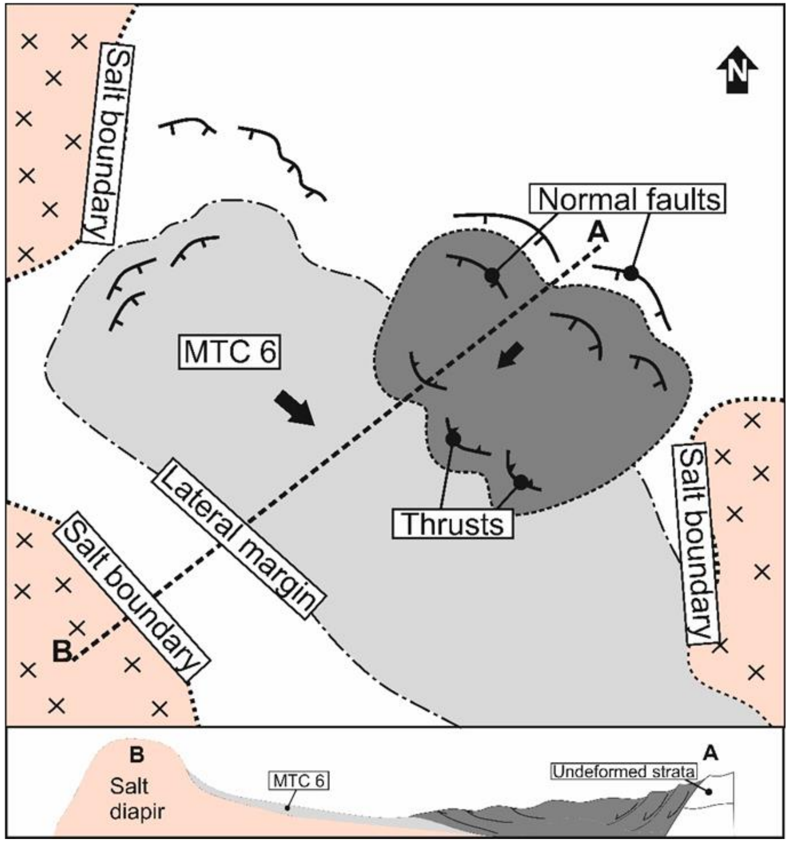

Figure 17

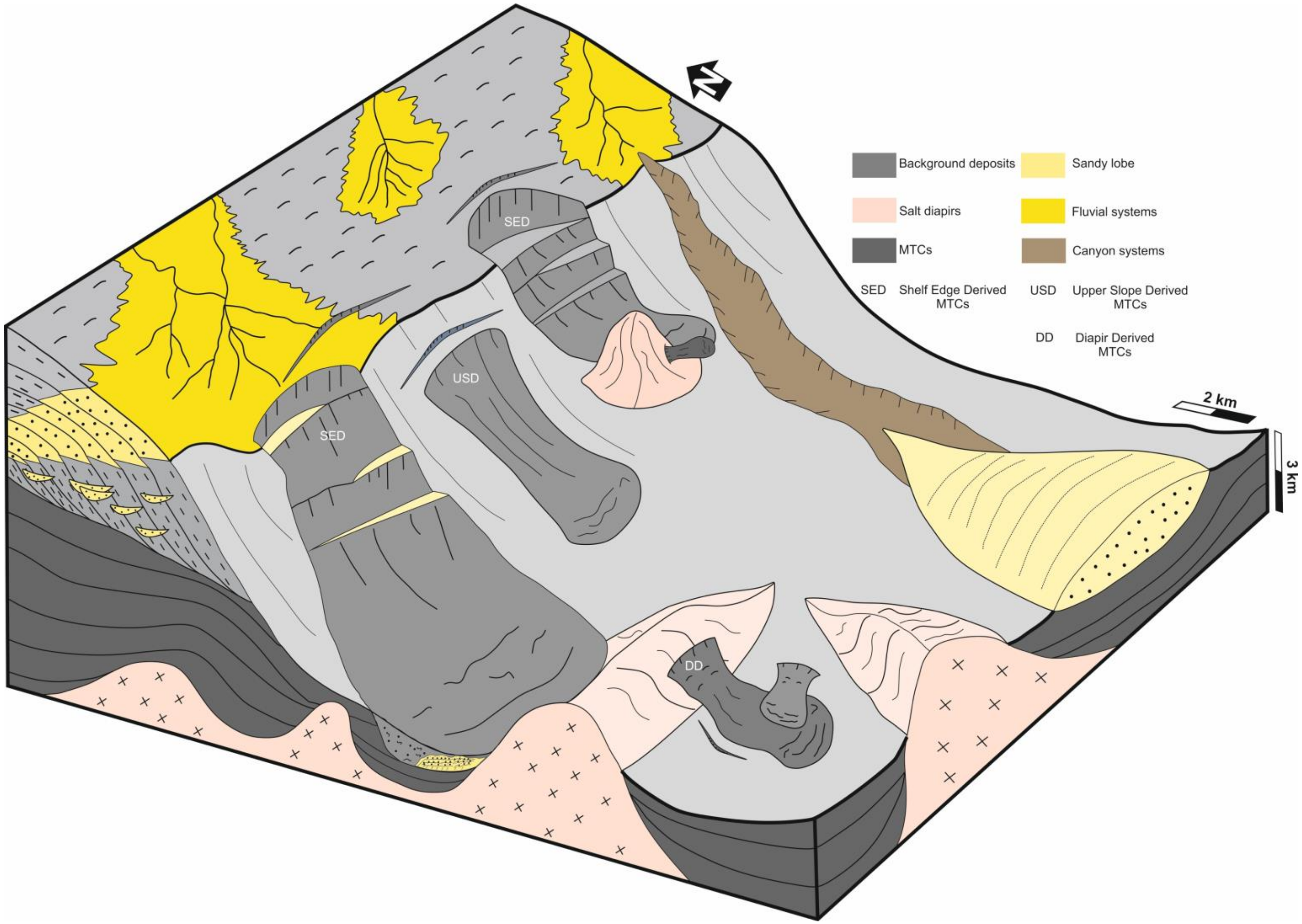

SED
SED
USD
DD
Background deposits
Sandy lobe
Salt diapirs
Fluvial systems
MTCs
Canyon systems
SED Shelf Edge Derived MTCs
USD Upper Slope Derived MTCs
DD Diapir Derived MTCs
2 km
3 km
N

Figure 18

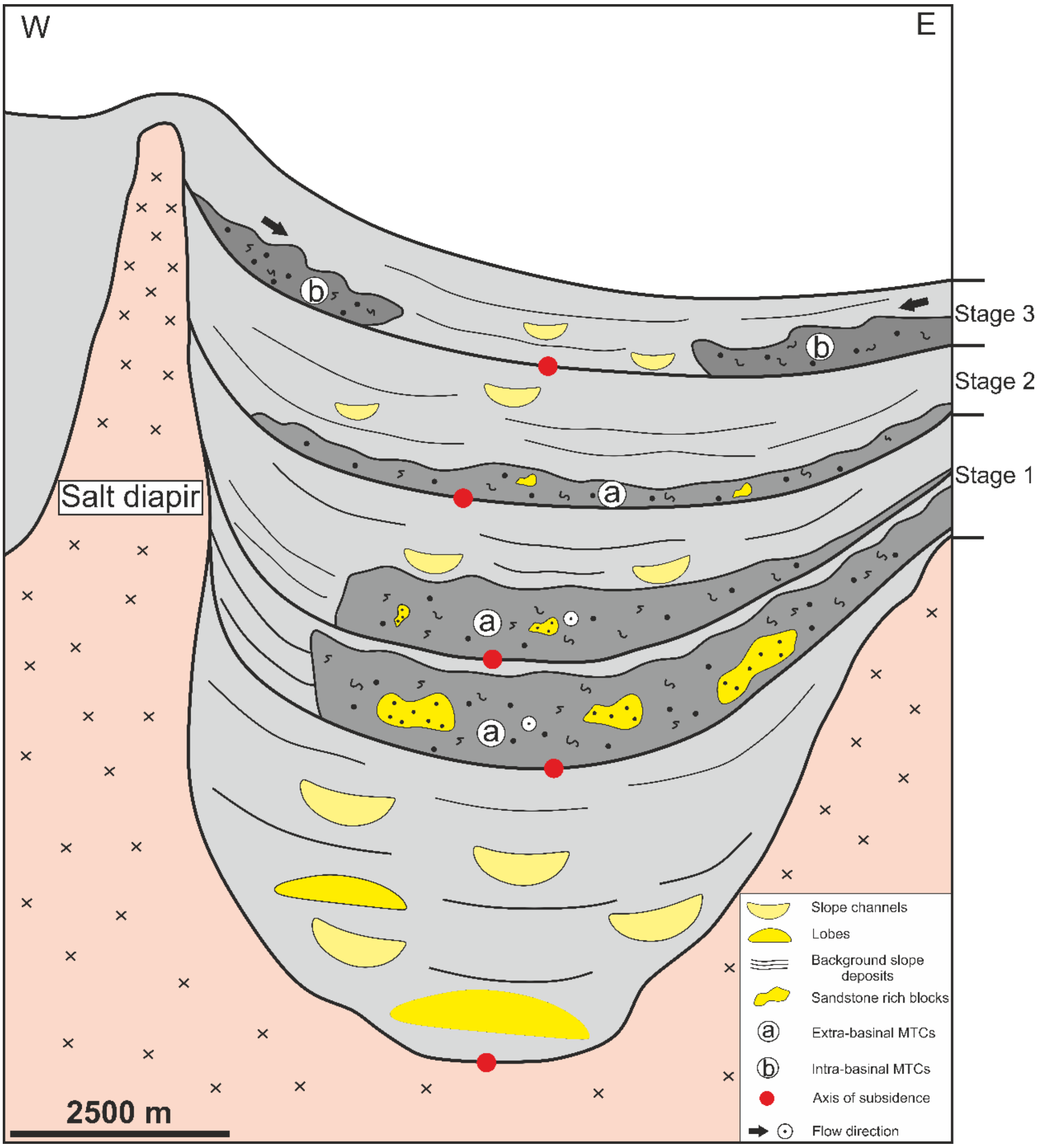

W
E
Stage 3
Stage 2
Stage 1
Salt diapir
2500 m
Slope channels
Lobes
Background slope deposits
Sandstone rich blocks
Extra-basinal MTCs
Intra-basinal MTCs
Axis of subsidence
Flow direction

Figure 19

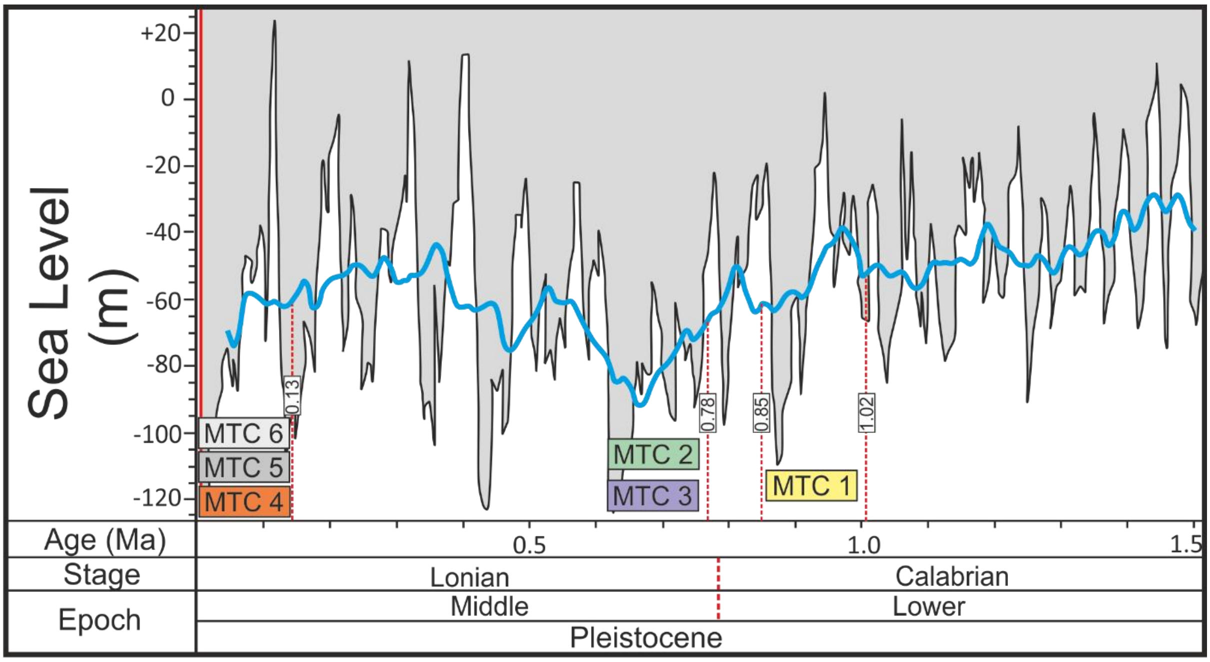

Sea Level (m)
+20
0
-20
-40
-60
-80
-100
-120
0.13
0.78
0.85
1.02
MTC 6
MTC 5
MTC 4
MTC 2
MTC 3
MTC 1
Age (Ma)
0.5
1.0
1.5
Stage
Lonian
Calabrian
Epoch
Middle
Lower
Pleistocene